Human neurons undergo protracted functional maturation into adulthood

Matthijs B. Verhoog[1,2,#], Roxanne M. Hattingh[1,2], Tariro Chatiza[1,2], Nawaal Samsodien[1,2], Yanelisa Pulani[1,2], Amalia N. Awala[1,2], Jared Tavares[7], Eline J. Mertens[8], Christiaan P. J. De Kock[8], Björn Kampa[10,11], Tim Kroon[8], Huibert D. Mansvelder[8,9], Ursula K. Rohlwink[2,3], Anthony Figaji[2,3], Graham Fieggen[2,3], Sean Tromp[2,3,5], Johannes M. N. Enslin[2,3], Roger Melvill[3,5], James Butler[2,4,5], Joseph V. Raimondo[1,2,6,#]

[#]corresponding authors: matthijs.verhoog@uct.ac.za & joseph.raimondo@uct.ac.za

Affiliations

[1]Division of Cell Biology, Department of Human Biology, University of Cape Town, Cape Town, South Africa

[2]Neuroscience Institute, University of Cape Town, Cape Town, South Africa

[3]Division of Neurosurgery, Department of Surgery, University of Cape Town, Cape Town, South Africa

[4]Division of Neurology, Department of Medicine, University of Cape Town, Cape Town, South Africa

[5]Epilepsy Surgery Unit, Mediclinic Constantiaberg Hospital, Cape Town, South Africa

[6]Wellcome Centre for Infectious Disease Research in Africa, Institute of Infectious Disease and Molecular Medicine, University of Cape Town, Cape Town, South Africa

[7]Department of Statistics, University of Cape Town, Cape Town, South Africa

[8]Department of Integrative Neurophysiology, Center for Neurogenomics and Cognitive Research, Vrije Universiteit Amsterdam, The Netherlands.

[9]Department of Neurology, Epileptology, Uniklinik RWTH Aachen, Germany

[10]Department of Systems Neurophysiology, Institute of Zoology, RWTH Aachen University, Germany

[11]JARA Brain Institute of Neuroscience and Medicine (INM-10), Forschungszentrum Jülich, Germany

Summary Paragraph

Human cognitive development is uniquely prolonged[1–3], reflecting the extended postnatal maturation of the cerebral cortex where cell-type differentiation[4,5], synaptogenesis[6,7], myelination[8] and transcriptional regulation[5,9,10] all follow protracted developmental timelines. However, when human cortical neurons reach functional electrophysiological maturity and how their developmental trajectory compares to other species remains unknown. Here we show through patch-clamp recordings of human temporal cortex from infancy to adulthood that supragranular pyramidal neurons exhibit pronounced neoteny of their functional properties, with physiological maturation continuing well into adulthood. Comparing human and mouse developmental trajectories reveals human neurons are on a much slower developmental timeline, maturing physiologically hundreds of times slower than mouse and 2-6 times slower than would be predicted from anatomical brain growth differences between species.

This reflects a fundamentally different allometric relationship between physiological and anatomical maturation; while mouse neuronal physiology closely tracks brain growth, human physiological development follows its own extended timeline. This slow maturation results in different stages of cognitive development being supported by functionally distinct neuronal populations, with the progression from infancy to middle age characterized by specific electrophysiological profiles. Notably, a neuronal subtype thought to be human-specific, with electrophysiological traits that enhance computational capacity, appears only in late adolescence or early adulthood. This extreme protraction of neurophysiological development provides a cellular basis for prolonged human cognitive maturation, demonstrating that neuronal physiological neoteny represents a fundamental evolutionary adaptation in human brain development.

Key words

Human electrophysiology, neuronal neoteny, physiological maturation, allometric scaling, supragranular pyramidal neurons, temporal cortex

Extended neuronal maturation in humans

To establish the nature and time course of physiological development in human cortical neurons, we performed whole-cell patch-clamp recordings in surgically resected brain tissue from subjects spanning infancy to adulthood (n = 584 cells, 80 subjects, 10 months to 55 years, Fig. 1a, Fig. S1, Table S1). We focused exclusively on pyramidal neurons in the upper, 'supragranular' layers of temporal association cortex, which exhibit enriched glutamatergic cell-type diversity with emerging human-specific specialisations and developmentally regulated programs linked to cognition[11,12]. Developmental trajectories of a range of electrophysiological features were captured with generalized linear mixed effects models (GLMMs), which allowed modeling age-dependent changes in mean and variance, while accounting for the hierarchical structure of our data, inter-subject variability, and covariates such as biological sex and cortical depth (Fig. 1b-f, Fig. S1-3). To enable cross-species comparison, we analyzed mouse supragranular cortical pyramidal neurons using the same approach (n = 562 cells, 242 mice, 0.8-65 days). We found clear conservation in the nature of physiological changes and their relative maturation order between species (Fig. 1b-f, h). However, the timescales differed dramatically: most mouse features reached mature levels within 2-4 weeks, while comparable maturation in humans required 2-4 decades (Fig. 1g, Fig. S2c).

Membrane resistance and time constant, which are fundamental properties that determine a neuron's sensitivity to inputs and temporal integration, showed slow, steady decreases with age in humans, reducing to approximately half their infant values over the first three decades of life (Fig. 1b,c, Fig. S2). Similar developmental decreases occurred in mice, albeit on a compressed timescale. These changes were accompanied by pronounced developmental decreases in variability in both species (Fig 1b,c, Fig. S3, Table S3). In humans, this primarily reflected reductions in within-subject variance rather than between-subject differences (Fig. S3d-f).

Human supragranular neurons uniquely express HCN channels, which impact temporal integration through the characteristic voltage "sag" response to hyperpolarization[13,14]. This feature, absent in mouse, was minimally present during childhood and progressively increased into adulthood (Fig. 1d). Notably, as sag ratio increased, so did its variability, suggesting late HCN channel expression contributes to adult physiological diversity (Fig. 1d, Fig. S2). In line with a growing influence of HCN channels on neuronal membrane properties, we observed changes in subthreshold filtering properties: both resonant frequency and cutoff frequency increased significantly with age (Fig. S8a-b), indicating that mature neurons become tuned to higher frequency oscillations and can process signals across a broader frequency range. These changes in frequency selectivity potentially enable adult neurons to better participate in the faster brain rhythms associated with mature cognitive functions.

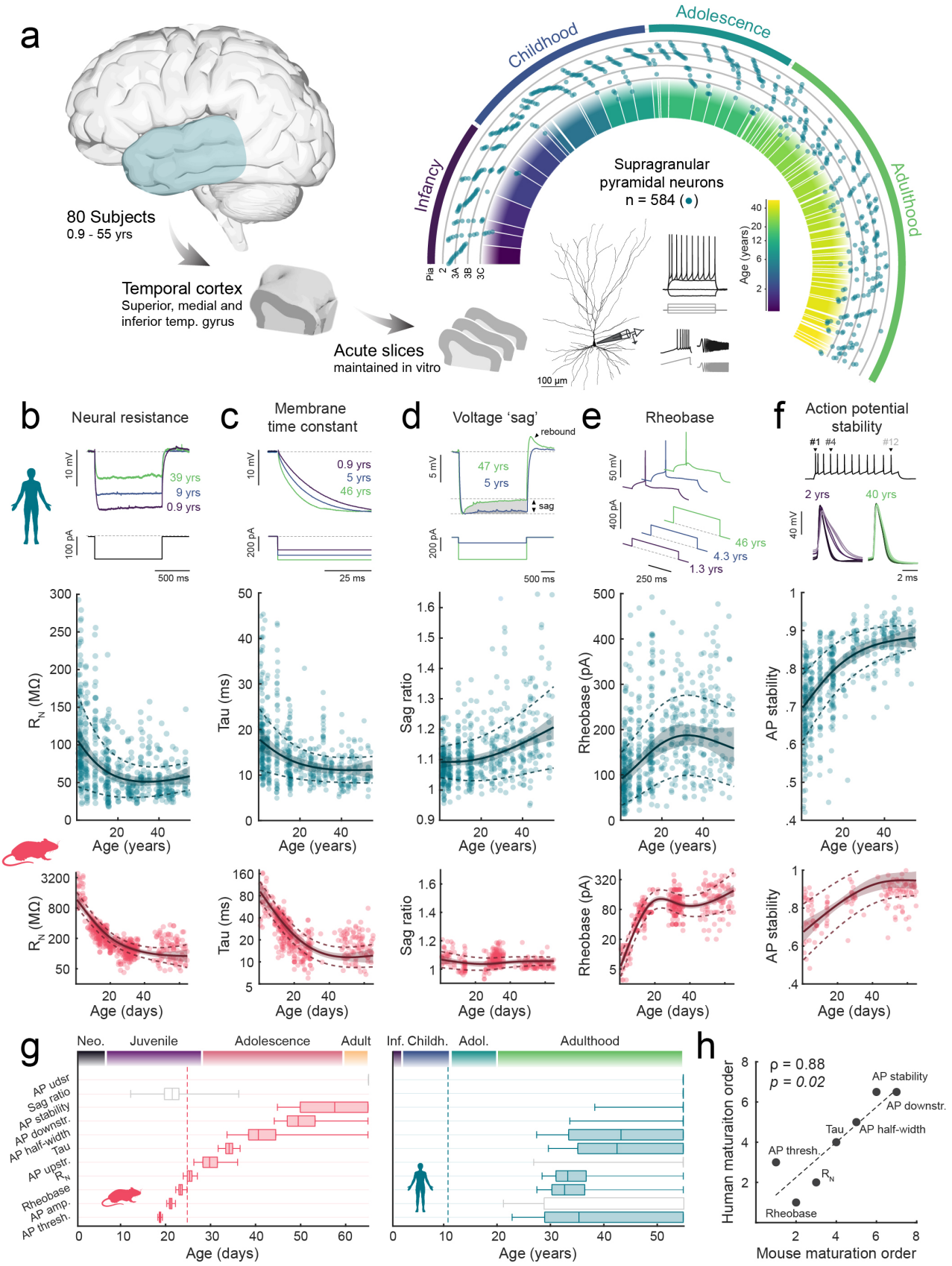

Fig. 1. Human cortical pyramidal neurons have extended postnatal maturation trajectories. a, Experimental pipeline for characterization of human pyramidal neuron physiology in neurosurgical samples of temporal cortex. Neurons were targeted for whole-cell patch-clamp recordings throughout supragranular layers 2-3C, from infancy to adulthood. **b-f**, Developmental trajectories of neural properties fit with GLM models for human (middle) and mouse (bottom) features. Each dot represents measure from single neuron. GLMM predicted mean and ± 95% confidence intervals shown by solid line and shading, dashed fits show standard deviation. Top traces show representative examples at different ages. Some y-axes are truncated for display purposes, full dataset presented in figure S3. **g**, Maturation peaks for mouse and human physiological features. Boxplots show bootstrap replicate median and IQR of peak maturation ages, whiskers mark the 2.5 and 97.5 percentiles. Boxplots are grey for features that did not show a significant age effect in the GLM model. Vertical dashed line indicates peak brain volume age. **h**, Maturation order of physiological features is conserved between human and mouse (Spearman's rank correlation, $p = 0.02$).

Suprathreshold features also displayed markedly prolonged developmental trajectories in humans compared to mice. Rheobase (the minimum current needed to elicit an action potential) slowly increased over the first few decades of human life, indicating gradual changes in neuronal excitability (Fig. 1e, Fig. S2). Mice showed parallel developmental increases in rheobase, but completed maturation within the first month.

Action potential stability (the capacity to sustain rapid kinetics during repetitive firing) represents the most protracted developmental feature in both species. Juvenile neurons in humans and mice exhibited pronounced use-dependent dampening of action potential waveforms, a phenomenon that gradually resolved with age (Fig 1f, Fig. S4). However, while mice achieved stable action potentials before adulthood, humans required decades longer, with stability only established in middle adulthood. This extended maturation timeline is particularly significant given that stable, rapid action potential kinetics have previously been linked to enhanced information processing and cognitive performance in humans[15].

Throughout development, human supragranular pyramidal neurons maintained their characteristic physiological heterogeneity[12,13,16–18], with properties like membrane sag varying systematically by position within layers[13,14]. Our models incorporated somatic depth as a significant predictor for all measured electrophysiological features, revealing robust layer-specific differences that persisted throughout development (Fig. S3b).

Together, these results demonstrate that while the fundamental patterns of neuronal maturation are conserved between mice and humans, human neurons undergo physiological changes on a dramatically extended timeline that continues well into adulthood.

Species-specific allometric growth rules

Larger brains have extended maturation periods, so the prolonged course of human physiological development might be anticipated based on our encephalization. However, whether neuronal physiology actually develops in proportion to brain growth remains an open question. To address this, we compared the normalized developmental trajectories of physiological features to brain growth curves in both humans and mice. In mice, we found that physiological maturation closely tracks brain growth, with most features reaching adult levels around the time maximum brain volume was attained (Fig. 1g, Fig. 2a). In humans, however, we observed a remarkable divergence: physiological maturation continued far beyond peak brain volume, with substantial developmental changes occurring long after brain growth has peaked (Fig. 1g, Fig. 2a).

To directly quantify the temporal differences in developmental trajectories between species, we employed dynamic time warping (DTW) analysis to align brain and physiological maturation curves (Fig. 2b-c, Fig. S2d). This revealed consistent linear warping paths, demonstrating that human and mouse developmental trajectories can be mapped to each other using constant scale factors (Fig. 2c). These scaling relationships varied by physiological feature, for example 1 mouse day corresponded to 385 human days (1.05 years) for action potential stability and 704 human days (1.93 years) for rheobase (Fig. 2c). When we performed the same analysis on brain volume growth curves, we found a substantially smaller scale factor: 1 mouse day corresponded to just 165 days (0.5 years) human days of brain development (Fig. 2b). Normalizing physiological scale factors by this volumetric brain growth ratio revealed that neurophysiological development in humans proceeds 2-6 times slower than would be predicted based solely on differences in brain growth rates (Fig. 2d).

This differential scaling suggests an uncoupling of physiological and anatomical maturation in humans, reflecting altered underlying allometric growth rules. During development, an organism's traits typically mature at predictable rates relative to one another, following power law relationships[19,20]. To explore whether such relationships may exist between neural physiology and overall brain maturation, we analyzed how physiological features vary with brain volume on logarithmic scales. Indeed, many features scaled linearly with brain volume, where the slope represented the allometric scaling exponent (α) capturing the rate of relative maturation (Fig. 2e).

Mice exhibited consistently strong allometric relationships with brain volume, characterized by high (absolute) α and R^2 values, indicating that neuronal physiology is tightly coupled to brain growth. In contrast, humans displayed substantially lower (absolute) α values and weaker allometric relationships (lower R^2 values) across multiple physiological features (Fig. 2e). This relative uncoupling allows human supragranular neuronal physiological maturation to follow its own extended developmental trajectory, proceeding more slowly than brain anatomical maturation.

Protracted e-type specialization

The slow developmental trajectories observed in humans extend neuronal maturation through multiple stages of cognitive development[3]. To test whether these stages therefore rely on physiologically different neurons, we performed multivariate analysis of 25 features including subthreshold intrinsic properties, action potential (AP) kinetics, stability, and firing patterns over four broad developmental age categories. This revealed significant differences in multivariate physiology (PERMANOVA: $F_{3,398} = 37.3$, $p < 0.001$, $R^2 = .21$, n = 403; all pairwise comparisons $p < 0.01$), demonstrating that different stages of cognitive development are supported by functionally distinct neural populations.

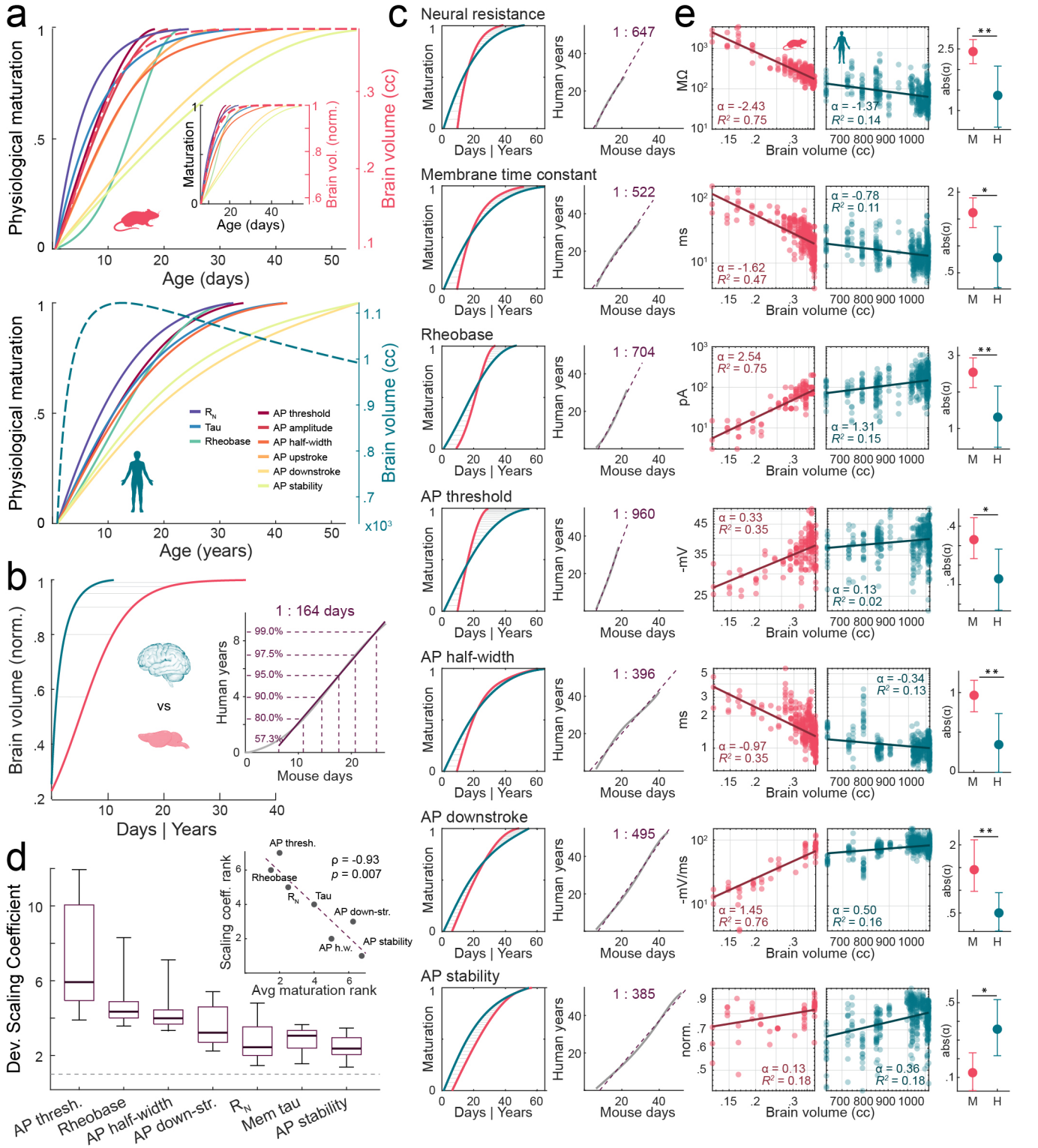

Fig. 2. Human physiological development trajectories are uncoupled from brain growth. a, Normalized developmental trajectories for mouse (top) and human (bottom) physiological features that showed age-dependent change, with concurrent anatomical brain growth. Inset: mouse physiological development over equivalent range of brain growth sampled in humans. **b**, Dynamic time warping analysis of human and mouse brain development curves. Inset: warping path mapping mouse days to human years (grey), corresponding brain volumes indicated by dashed lines. Slope of linear fit yielded the mouse-to-human brain development scale factor. **c**, Cross-species DTW analysis of developmental trajectories. Note that all physiological scale factors were much greater than the brain growth scale factor. **d**, Developmental scaling coefficients derived from ratio of physiological to anatomical scale factors, ordered by maturation rank. Inset: correlation between developmental scaling coefficient and maturation rank. **e**, Allometric scaling relationships between physiological features and brain volume during brain growth phase. Allometric scaling exponent α was derived from the slope of the linear fit to log-log scaled data (methods). Each dot represents recorded data from a single neuron, with subject age transformed to expected brain volume. Right panels: absolute α values for human and mouse (bootstrap median ± 2.5-97.5% percentiles; *$p < 0.05$, **$p < 0.01$).

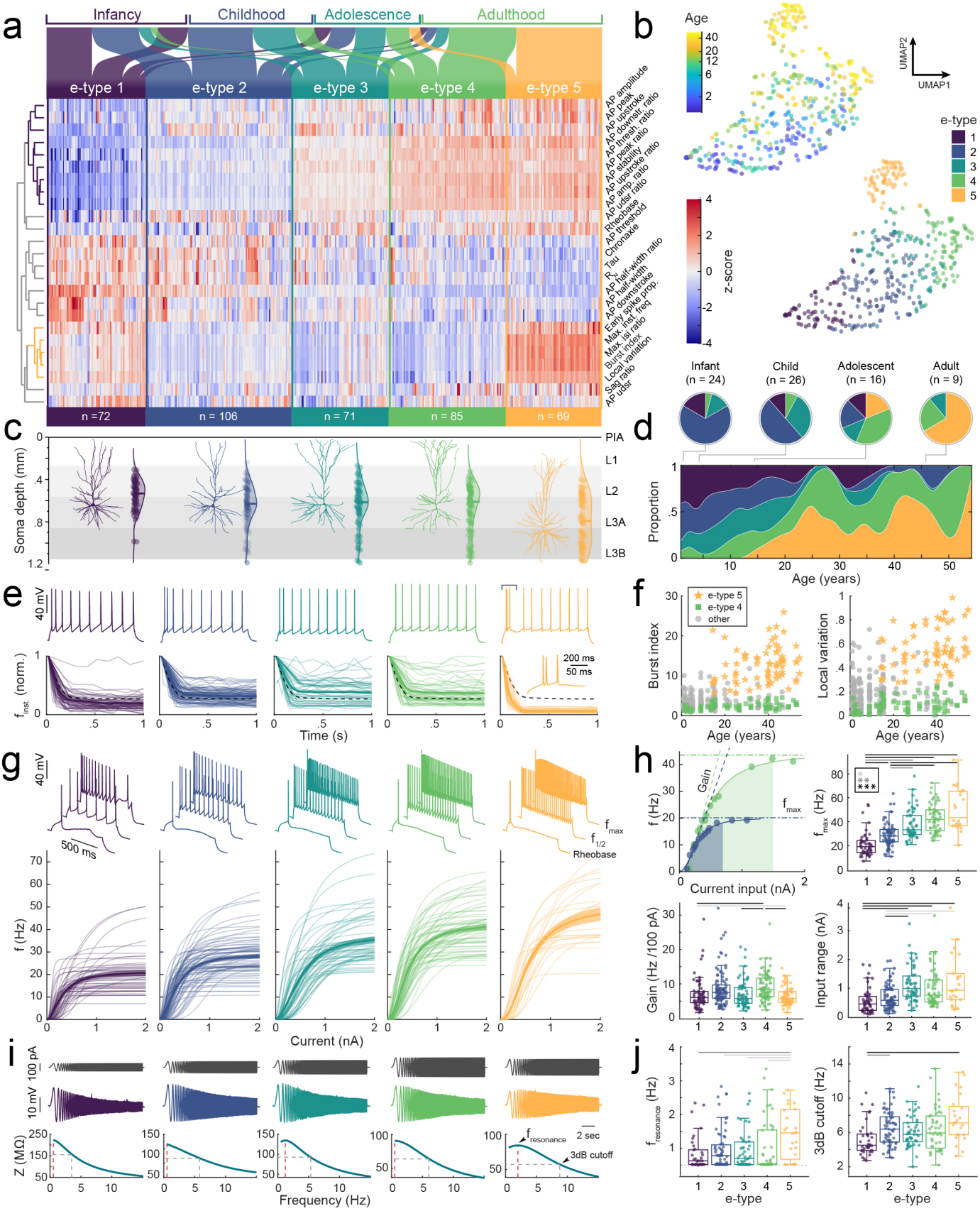

Fig. 3. Slow emergence of physiological phenotypes with distinct input-output properties. a, Gaussian mixture modelling cluster analysis. Z-scored physiological features (rows) for individual neurons grouped by e-type classification. Top alluvial diagram maps e-types to age categories. Left: Hierarchical feature dendrogram, purple subtree: AP waveform/ stability features, orange subtree: firing regularity. **b**, UMAPs colored by age and e-type. **c**, Soma depth of e-types and example reconstructions. **d**, Changes in e-type composition with age. Pie charts show e-type composition of individual subjects. **e**, E-type firing patterns. Example AP trains and normalized instantaneous firing frequency ($f_{inst.}$, thick: e-type average, dashed: pop. average). **f**, Age-related changes in firing regularity. **g**, E-type input-output relationships. Top: Example traces at rheobase, half-max firing rate, and max firing rate. Bottom: Input-output (*f-I*) curves of individual neurons with overlaid mean ± s.e.m. **h**, *f-I* curve features across e-types. Significance levels shown by black ($p < 0.001$), grey ($p < 0.01$) or light grey ($p < 0.05$) lines. **i**, E-type subthreshold filtering properties. Top-bottom: Chirp current injection protocol, corresponding voltage responses and impedance amplitude profiles with resonant and 3dB cutoff frequencies. **j**, Summary box plots of e-type filter properties. E-type 5 neurons have higher resonant frequency than all other e-types.

To understand whether neurons mature along specific paths through multivariate space, identify putative developmental states and determine when the distinct electrophysiological types identified in the adult cortex emerge[12,17], we performed Gaussian mixture modeling (GMM) on our multivariate physiological dataset. This unsupervised clustering approach revealed five electrophysiological signatures (e-types) whose prevalence shifted systematically during development, forming a continuous maturation gradient in UMAP space, with progressively increasing median age from e-type 1 to 5 (Fig. 3a,b,d). Multiple e-types were typically present within individual subjects (Fig. S5f) and were interspersed throughout the supragranular layers (Fig. 3c, Fig. S5g).

E-type 1, common in infants, exhibited slow AP kinetics and unstable waveforms, while e-types 2 and 3 represented intermediate physiological states typical of childhood and adolescence. Adult cortex predominantly featured e-types 4 and 5, which had mature characteristics like low membrane resistance, fast time constants, and stable APs but differed significantly in firing patterns (Fig. 3a,e-f); e-type 4 showed regular firing, whereas e-type 5 displayed initial bursts of multiple APs, significantly altering spike train regularity measures (Fig. S6). The presence of a subpopulation of burst-firing neurons in the deeper supragranular layers has been previously reported in adult humans[12,17], and appears to be a species-specific developmental endpoint absent in mouse cortical L2/3 (Fig. S6). Trajectory analysis demonstrated a developmental progression from infant e-type 1 towards adult e-types 4 and 5, with the divergence in firing patterns appearing late in maturation (Fig. 3f, Fig. S6).

To understand the functional consequences of developmental shifts in e-type composition, we explored computational properties that were not included in the clustering analysis. E-type classification corresponded to significant changes in neuronal input-output relationships, characterized by progressively increased maximum firing frequency and enhanced input range from e-type 1 to 5 (Fig. 3g-h). Interestingly, the slope of the f-I curve was higher in e-types 2 and 4, while e-types 1, 3, and 5 showed similar gain values despite major electrophysiological differences (Fig. 3g-h, Fig. S7). We hypothesized that the emergence of burst-firing e-type 5 neurons might coincide with the late developmental expression of HCN channels. Indeed, voltage sag, a hallmark of HCN channel activity, was significantly elevated in e-type 5 compared to other e-types (Fig. S8d). Consistent with enhanced HCN expression, e-type 5 neurons exhibited higher resonant and cutoff frequencies and markedly lower impedance across the entire frequency range tested (Fig. 3i-j, Fig. S8e-f), reflecting their reduced membrane resistance and faster time constants.

These findings reveal that human cortical neuron development involves an extended, continuous progression characterized by distinct electrophysiological profiles and computational capabilities at different stages. The unique emergence of burst-firing neurons with pronounced HCN-mediated resonance in adults may provide specialized computational features supporting advanced cognitive functions.

Discussion

Our extensive electrophysiological dataset, comprising over 1100 patch-clamp recordings from human and mouse supragranular cortical neurons across comparable developmental periods, reveals a profound species-specific divergence in neuronal maturation. While the fundamental sequence of physiological changes is conserved, human cortical neurons exhibit a striking neoteny in their development. Unlike prior rodent[21–25] and human[26] studies that characterized cortical electrophysiological maturation across discrete developmental stages, we captured the underlying developmental trajectories of physiological features and interpret these against the backdrop of brain-volume growth. In mice, this revealed a tight coupling between anatomical and physiological development, suggesting a stable ontogenetic allometric relationship that may characterize typical mammalian neurodevelopment. In stark contrast, human supragranular neurons follow a remarkably protracted trajectory where physiological maturation continues for decades beyond the completion of volumetric brain growth, proceeding 2-6 times slower than would be predicted from cross-species brain size differences alone and consistent with extended human cognitive development[3]. This ontogenetic divergence parallels recent findings that adult human neurons are also outliers in static allometric relationships, exhibiting lower ionic conductances than predicted by their size compared to other mammals[27], suggesting that human neuronal distinctiveness extends across both developmental and mature functional domains.

Long-standing models of post-natal cognitive development have typically regarded mature information processing as the outcome of synaptic and circuit-level mechanisms[28,29,7], implicitly assuming that the intrinsic electrical properties of individual neurons remain largely unchanged. Our results revise this assumption, revealing that intrinsic functional properties continue to mature on a distinct, protracted timeline. Whilst recent work has demonstrated that human supragranular intrinsic properties continue to change after birth[26], the developmental trajectories and timing remained unclear. Our comprehensive dataset allowed us to quantify the detailed maturational timeline of each physiological feature and reveal that the sequence of functional development is remarkably conserved between species, but dramatically extended in humans. While numerous studies have documented human neoteny at cellular and molecular levels (through extended synaptogenesis, delayed myelination, and protracted gene expression dynamics[4–8,10]) our findings establish precisely when the functional properties of cortical neurons mature throughout postnatal development. This neurophysiological neoteny likely provides a cellular substrate for supporting the extended development of human cognitive functions[1,2].

The systematic decrease in physiological variability with age in both species, particularly through reductions in within-subject variance in humans, suggests a developmental progression from more plastic, variable neuronal states toward more stable, specialized functional profiles. The juvenile neuronal properties we identified in humans (high input resistance, long membrane time constants, and slower action potentials) result in neurons that are markedly more excitable and responsive to small inputs, but with limited precision or speed. Analogous to the concept of dropout in artificial neural networks, this early variability and noisiness might prevent overfitting during critical developmental learning periods, promoting robust generalization later in life[30]. As development progresses, membranes become leakier and faster, action potentials narrow and accelerate, and rheobase increases. These transformations convert neurons from highly excitable but imprecise computational elements into selective, rapidly responding units capable of sustaining higher firing frequencies with greater temporal precision. Thus, this developmental trajectory likely optimizes cortical circuits first for maximal plasticity and broad learning during childhood, followed by the stability and precision required for reliable information processing, mature executive function, and higher-order cognition[31].

Beyond merely delaying maturation, human neuronal development also culminates in physiological specializations absent in mice. The emergence of distinctive adult e-types, particularly the burst-firing neurons of e-type 5, represents a species-specific endpoint of human cortical development that aligns with transcriptomic characterizations identifying unique neuron transcriptomic subtypes, such as CARM1P1 and deep FREM3[12]. These neurons, which appear only in adulthood, exhibit enhanced frequency selectivity through their resonance properties, a physiological signature previously linked to enhanced information processing in multiplexed neural codes[32]. Given that HCN channels regulate dendritic integration and network rhythmogenesis[33,34], their late emergence could endow mature human cortical circuits with unique integrative capabilities supporting complex cognitive functions like working memory[35,36]. Importantly, we show that features previously identified as distinctly primate or human, including supragranular burst firing, fast and stable action potentials and pronounced HCN expression[12,13,15], emerge only after extended postnatal development.

The protracted nature of human neuronal development aligns with evidence from pluripotent stem cell studies showing that human neurons maintain their slow physiological maturation even after xenotransplantation into mouse cortex[37]. Recent findings suggest this extended timeline is controlled by epigenetic developmental barriers that constrain the pace of maturation[9]. Together with our observations, this supports the view that neuronal neoteny represents a fundamental evolutionary adaptation rather than a simple byproduct of increased brain size.

Our findings have important implications for translational neuroscience. The substantial temporal divergence between mouse and human developmental trajectories necessitates careful consideration when modeling human neurodevelopmental disorders in rodents. Notably, much rodent electrophysiology is performed on two-week-old animals[38], corresponding to middle childhood in humans for many physiological features. Our developmental mapping provides a mechanism for selecting age-appropriate animal models for specific human developmental stages.

By demonstrating that different stages of human cognitive development are supported by functionally distinct neuronal properties, our work establishes that the tempo of neuronal maturation is likely critical for brain development and health. This evolutionary-extended timeline appears calibrated to support the progressive acquisition of complex cognitive functions. Perturbations of this schedule may seed neurodevelopmental disorders: premature maturation could truncate periods of heightened plasticity, whereas delayed maturation might impair the precise temporal dynamics needed for higher cognition. Disorders that surface only later in life may stem from latent timing irregularities that escape detection until circuits demand fully mature properties. More broadly, our data indicate that developmental timing, together with circuit topology and cellular heterogeneity, constitutes a fundamental evolutionary axis shaping the human brain and offers a framework for interpreting both the emergence of human cognitive capacities and the characteristic ages at which developmental brain disorders arise.

References

1. Silbereis, J. C., Pochareddy, S., Zhu, Y., Li, M. & Sestan, N. The Cellular and Molecular Landscapes of the Developing Human Central Nervous System. *Neuron* **89**, 248–268 (2016).
2. Workman, A. D., Charvet, C. J., Clancy, B., Darlington, R. B. & Finlay, B. L. Modeling transformations of neurodevelopmental sequences across mammalian species. *J Neurosci* **33**, 7368–7383 (2013).
3. Piaget, J. Intellectual Evolution from Adolescence to Adulthood. *Human Development* **15**, 1–12 (2009).
4. Fung, S. J. *et al.* Expression of Interneuron Markers in the Dorsolateral Prefrontal Cortex of the Developing Human and in Schizophrenia. *AJP* **167**, 1479–1488 (2010).
5. Velmeshev, D. *et al.* Single-cell analysis of prenatal and postnatal human cortical development. *Science* **382**, eadf0834 (2023).
6. Charrier, C. *et al.* Inhibition of SRGAP2 function by its human-specific paralogs induces neoteny during spine maturation. *Cell* **149**, 923–935 (2012).
7. Petanjek, Z. *et al.* Extraordinary neoteny of synaptic spines in the human prefrontal cortex. *Proceedings of the National Academy of Sciences* **108**, 13281–13286 (2011).
8. Miller, D. J. *et al.* Prolonged myelination in human neocortical evolution. *Proceedings of the National Academy of Sciences* **109**, 16480–16485 (2012).
9. Ciceri, G. *et al.* An epigenetic barrier sets the timing of human neuronal maturation. *Nature* **626**, 881–890 (2024).
10. Somel, M. *et al.* Transcriptional neoteny in the human brain. *Proceedings of the National Academy of Sciences* **106**, 5743–5748 (2009).
11. Steyn, C. *et al.* A temporal cortex cell atlas highlights gene expression dynamics during human brain maturation. *Nat Genet* **56**, 2718–2730 (2024).
12. Berg, J. *et al.* Human neocortical expansion involves glutamatergic neuron diversification. *Nature* **598**, 151–158 (2021).
13. Kalmbach, B. E. *et al.* h-Channels Contribute to Divergent Intrinsic Membrane Properties of Supragranular Pyramidal Neurons in Human versus Mouse Cerebral Cortex. *Neuron* **100**, 1194-1208.e5 (2018).
14. Chameh, H. M. *et al.* Sag currents are a major contributor to human pyramidal cell intrinsic differences across cortical layers and between individuals. 1–26 (2019).
15. Testa-Silva, G. *et al.* High Bandwidth Synaptic Communication and Frequency Tracking in Human Neocortex. *PLoS Biology* **12**, e1002007 (2014).
16. Deitcher, Y. *et al.* Comprehensive Morpho-Electrotonic Analysis Shows 2 Distinct Classes of L2 and L3 Pyramidal Neurons in Human Temporal Cortex. *Cerebral Cortex* 1–17 (2017) doi:10.1093/cercor/bhx226.
17. Planert, H. *et al.* Intra-individual Physiomic Landscape of Pyramidal Neurons in the Human Neocortex. *bioRxiv* 2021.11.08.467668 (2021).
18. Kushner, J. K. *et al.* Characterizing the Diversity of Layer 2/3 Human Neocortical Neurons in Pediatric Epilepsy. *eNeuro* **12**, ENEURO.0247-24.2025 (2025).
19. Gould, S. J. ALLOMETRY AND SIZE IN ONTOGENY AND PHYLOGENY. *Biological Reviews* **41**, 587–638 (1966).
20. Huxley, J. *Problems of Relative Growth*. (L. MacVeagh, The Dial Press, New York, 1932). doi:10.5962/bhl.title.6427.
21. Kroon, T., van Hugte, E., van Linge, L., Mansvelder, H. D. & Meredith, R. M. Early postnatal development of pyramidal neurons across layers of the mouse medial prefrontal cortex. *Sci Rep* **9**, 5037 (2019).
22. Zhang, Z. Maturation of Layer V Pyramidal Neurons in the Rat Prefrontal Cortex: Intrinsic Properties and Synaptic Function. *Journal of Neurophysiology* **91**, 1171–1182 (2004).
23. Picken Bahrey, H. L. & Moody, W. J. Early Development of Voltage-Gated Ion Currents and Firing Properties in Neurons of the Mouse Cerebral Cortex. *Journal of Neurophysiology* **89**, 1761–1773

(2003).
24. Kasper, E. M., Larkman, A. U., Lübke, J. & Blakemore, C. Pyramidal neurons in layer 5 of the rat visual cortex. II. Development of electrophysiological properties. *Journal of Comparative Neurology* **339**, 475–494 (1994).
25. McCormick, D. A. & Prince, D. A. Post-natal development of electrophysiological properties of rat cerebral cortical pyramidal neurones. *The Journal of Physiology* **393**, 743–762 (1987).
26. Barzó, P. *et al.* Electrophysiology and morphology of human cortical supragranular pyramidal cells in a wide age range. *eLife* **13**, RP100390 (2025).
27. Beaulieu-Laroche, L. *et al.* Allometric rules for mammalian cortical layer 5 neuron biophysics. *Nature* **600**, 274–278 (2021).
28. Paus, T. *et al.* Structural maturation of neural pathways in children and adolescents: in vivo study. *Science* **283**, 1908–1911 (1999).
29. Hensch, T. K. Critical period plasticity in local cortical circuits. *Nat Rev Neurosci* **6**, 877–888 (2005).
30. Srivastava, N., Hinton, G., Krizhevsky, A., Sutskever, I. & Salakhutdinov, R. Dropout: A Simple Way to Prevent Neural Networks from Overfitting. *Journal of Machine Learning Research* **15**, 1929–1958 (2014).
31. Mittermaier, F. X. *et al.* Membrane potential states gate synaptic consolidation in human neocortical tissue. *Nat Commun* **15**, 10340 (2024).
32. Naud, R. & Sprekeler, H. Sparse bursts optimize information transmission in a multiplexed neural code. *Proc Natl Acad Sci U S A* **115**, E6329–E6338 (2018).
33. Magee, J. C. Dendritic Hyperpolarization-Activated Currents Modify the Integrative Properties of Hippocampal CA1 Pyramidal Neurons. *J. Neurosci.* **18**, 7613–7624 (1998).
34. Stark, E. *et al.* Inhibition-induced theta resonance in cortical circuits. *Neuron* **80**, 1263–1276 (2013).
35. Wang, M. *et al.* Neuronal basis of age-related working memory decline. *Nature* **476**, 210–213 (2011).
36. Wang, M. *et al.* α2A-Adrenoceptors Strengthen Working Memory Networks by Inhibiting cAMP-HCN Channel Signaling in Prefrontal Cortex. *Cell* **129**, 397–410 (2007).
37. Linaro, D. *et al.* Xenotransplanted Human Cortical Neurons Reveal Species-Specific Development and Functional Integration into Mouse Visual Circuits. *Neuron* **104**, 972-986.e6 (2019).
38. Markram, H. *et al.* Reconstruction and simulation of neocortical microcircuitry. *Cell* **163**, 456–492 (2015).

Acknowledgements

We would like to thank patients, their parents and families for the generous donation of resected tissue for research purposes. We thank hospital clinical and support staff including Kelsey Bester, Lucretia van der Horst, Jodi Jacobs and Natalie Vincent for logistical support as well as members of the Raimondo Lab, Dorit Hockman, Rachael Dangarembizi, Christopher Dulla and Colin Akerman for advice and comments. We are grateful to Simon Weiler and Anne-Marie Oswald for sharing data from previously published mouse datasets. We thank Henry Markram (École Polytechnique Fédérale de Lausanne) and Tobias Boenhoffer (Max Planck Institute for Biological Intelligence) for generous donation of patch-clamp equipment to the UCT, Rodrigo Perrin, Charles Harris and Volker Staiger for assistance setting up of Ephys recording equipment and software, Caron Jacobs and the Africa Microscopy Initiative Imaging Centre (RRID: SCR_025881) for microscopy support and the UCT ICTS High Performance Computing team for support using the high performance cluster. This research received support from a European Molecular Biology Organisation Fellowship (EMBO ALTF 415-2018; MBV), a UCT Faculty of Health Sciences Fellowship (MBV), a Claude Leon Foundation Fellowship (MBV), a Royal Society Newton Advanced Fellowship (JVR), the SA National Research Foundation (JVR), the Blue Brain Project (JVR), the Gabriel Foundation (JVR), a Wellcome Trust Seed Award (214042/Z/18/Z) (JVR), the South African Medical Research Council (JVR) and the FLAIR Fellowship Programme (FLR\R1\190829) (JVR): a partnership between the African Academy of Sciences and the Royal Society funded by the UK Government's Global Challenges Research Fund and a Wellcome Trust International Intermediate Fellowship (222968/Z/21/Z) (JVR).

Methods

Human brain samples

Temporal cortex tissue was obtained from 80 donors (37 females, 43 males; 0.9-55 years) who underwent surgical treatment for epilepsy with various etiologies (Table S1). Tissue originated from the inferior, medial and superior gyrus of the temporal lobe, approximately 2–6 cm posterior to the temporal pole and was removed for access to deeper brain structures, or comprised the least affected, most normal tissue surrounding the primary affected area, lesion or tumor.

The cohort comprised 34 donors from South Africa of diverse ancestral backgrounds: 18 black African, 7 mixed ancestry, and 9 white/Caucasian individuals. The other 46 donors were from the Netherlands, for which ancestry information was unavailable but were likely predominantly white/Caucasian. These ancestry descriptors serve to illustrate the inclusion of underrepresented populations in our study sample, and play no role in participant recruitment, study design, analysis, or interpretation of results. All procedures on human tissue were performed with the approval of the Human Research Ethical Committee of the University of Cape Town (HREC Protocol 016/2018) and the Medical Ethical Committee of the VU University Medical Centre. Written informed consent was obtained prior to surgery from all patients, or in case of minors, from their guardians.

The mouse dataset was compiled from published datasets of L2/3 cortical pyramidal neuron physiology[1–6], supplemented with original recordings to sample the full postnatal developmental period from birth to adulthood. The pooled dataset included 561 neurons from 242 animals (P0.8-65, Table S2). All procedures for mouse neocortical brain slice preparation were approved by the Animal Research Ethics Committee of the University of Cape Town (AEC Protocol 021/026).

Brain slice preparation

Following resection, cortical tissue was transferred to ice-cold artificial cerebrospinal fluid (aCSF) containing (in mM): 110 choline chloride, 26 $NaHCO_3$, 10 D-glucose, 11.6 sodium ascorbate, 7 $MgCl_2$, 3.1 sodium pyruvate, 2.5 KCl, 1.25 NaH_2PO_4, and 0.5 $CaCl_2$, and transported to the laboratory within 10-20 minutes. Tissue blocks were embedded in low melting point agar for sectioning (350 µm) on a Compresstome (Precisionary Instruments) or processed for vibratome slicing as previously described[7,8]. Slices were stored at 34°C for 15-30 minutes, then allowed to recover for at least 1 hour at room temperature before recording in aCSF containing (in mM): 125 NaCl, 3 KCl, 1.25 NaH_2PO_4, 1 $MgSO_4$, 2 $CaCl_2$, 26 $NaHCO_3$, and 10 D-glucose. All solutions were continuously bubbled with carbogen (95% O_2, 5% CO_2) and maintained at 300 mOsm osmolarity. Mouse brain slices were prepared using identical procedures, with coronal frontal cortex sections obtained from C57Bl/6J mice following unanesthetized decapitation.

Characterization of neural physiology

Following recovery, slices were placed in a recording chamber and perfused with aCSF (3–4 ml/min, 31–34 °C). Pyramidal neurons in supragranular layers 2-3 were identified with oblique illumination or differential interference contrast microscopy. Whole-cell patch-clamp recordings were then made using borosilicate glass pipettes with fire-polished tips (4.0–6.0MΩ resistance) filled with intracellular solution containing (mM): 110 K-gluconate; 10 KCl; 10 HEPES; 10 K_2Phosphocreatine; 4 ATP-Mg; 0.4 GTP, biocytin 5mg/ml (pH adjusted with KOH to 7.3; 280–290 mOsm). Whole-cell patch-clamp recordings were made using Axopatch 200B or MultiClamp 700 A/B amplifiers (Axon Instruments), sampling at 10-50 kHz and low pass filtering at 5-10 kHz. Recordings were digitized with National Instruments ITC-1600 or Axon Digidata 1440A digitizers and acquired using PulseQ (v1.01, Funetics), WinWCP (v5.2.4, University of Strathclyde) or pClamp (v14, Axon Instruments) acquisition software.

Morphology & Histology

After recordings, slices were fixed in 4% paraformaldehyde overnight, rinsed with phosphate buffer (PB) and stored in PB-azide at 4°C. Biocytin-filled cells were visualized using either the avidin–biotin–peroxidase method[9] and mounted on slides and embedded in Mowiol, or by Alexa488-streptavidin (1:500, Thermo Fisher Scientific) for 48 hours at room temperature, followed by 3 washes in PB before being mounted in Vectashield (Vector Laboratories).

For histological assessment, recorded sliceswere co-stained with DAPI (4',6-diamidino-2-phenylindole, 5 µM) for 20 minutes at room temperature to visualize cell nuclei and cortical architecture and imaged on a Zeiss Axioscan 7 automated fluorescence slide scanner at 20x. Layer and cortical thickness was subsequently measured using ImageJ [10]. The distance of retrieved somata to pia was measured along the apical dendrite, and position within L2-3 was verified (Fig S1). For neurons not retrieved in post-hoc staining, the pia-soma distance measured during recording was used. Only neurons <1500 µm from pia were included in this study (range: 237-1500 µm, mean 765 µm).

A subset of cells was selected for full 3D reconstruction of neuronal morphology using Neurolucida software (MBF Bioscience). Z-stack mosaics were acquired at 0.5 µm intervals on a Zeiss LSM 880 Airyscan confocal microscope (Carl Zeiss, hosted by UCT Human Biology Dept.) or an LSM 980 Airyscan 2 (hosted by the African Microscopy Initiative (AMI)), using a 63× 1.4 NA oil-immersion objective (Fig. S1).

Electrophysiological feature extraction & analysis

Stimulation protocols

Recorded neurons were subjected to a suite of current clamp injection protocols to characterize a wide range of physiological properties. These included current injection steps, ramps and chirps of varying length and amplitude. The intensity of current stimuli was adjusted for each neuron, uniformly scaling protocols up or down to ensure neurons were driven to a similar degree regardless of input resistance. Neurons with V_{rest} close to firing threshold were hyperpolarized to -60 mV by applying a constant holding current to facilitate physiological characterization. Recordings with access resistance R_a > 30MΩ, unstable baselines or baselines >-55 mV were discarded. Data files were then analyzed using custom MATLAB scripts. All sweeps were visually inspected and cases where events (e.g. noise, spontaneous activity, sudden change in R_a) challenged the normal extraction of physiological features were excluded.

Basic physiological properties

Subthreshold membrane properties were calculated as follows[11] (Fig. S2): Input resistance R_N was the *I-V* slope of a linear fit to the minimum voltage deflection measured within 80 ms of onset of hyperpolarizing current injection (0.5-1s). Membrane time constant was the average time constant of single exponential fits (R^2 > 0.9) to the same hyperpolarizing current pulses. To obtain sag ratio, R_N was divided by resistance at steady state (R_{SS}, where both fits had R^2 > 0.8). Rheobase (Rb) and chronaxie (Cx) were estimated fitting the linear charge-delay relationship: $Q = Rb \times (delay + Cx)$[12,13], where charge Q was the product of AP delay and injected current. This approach allowed estimation or rheobase (slope) and chronaxie (-x intercept) from a diverse set of protocols or from cells where a limited number of suprathreshold responses were available (required: min 3 ms stimulus duration, ≥3 current levels, ≥3 sweeps, max 4 mV baseline change between sweeps and fit R^2 > 0.75). In a small subset of cells where fitting was not possible, rheobase was based on the minimum step current injection (≥500 ms) to elicit an AP.

Action potentials

Action potentials (APs) were detected as peaks exceeding 0 mV and threshold was defined as the voltage at which the derivative was last <15 mV/ms before the peak. (Fig. S4). Amplitude was the difference between threshold and peak voltage, and AP half-width measured as the ms time between AP rise and fall at V_{thresh} + ½ AP amplitude. Cells with half-width <0.5 ms were excluded as presumed interneurons. AP upstroke and downstroke were the max and minimum values of the AP derivative (mV/ms) during the rising and falling phase of the AP, the upstroke-downstroke ratio (AP udsr) was the absolute ratio of the two. The instantaneous firing frequency in Hz was $f_{inst} = \frac{1}{t - t_{prev}}$, where t_{prev} was the time of last spike.

The total pool of recorded APs exceeded 100,000. Although our AP detection and feature calculation algorithms performed well across ages and firing intensities, at high firing rates the reliability of AP detection methods can be compromised. We hence imposed broad quality control constraints for AP threshold (between -60 and 0 mV), amplitude (20-120 mV), half-width (0.5-10 ms), upstroke (0-800 mV/ms), downstroke (-250-0 mV/ms), and f_{inst} (<200 Hz). APs failing any of these criteria were excluded from analyses of AP kinetics, in addition to those recorded during high-intensity current injections aimed at pushing neurons to their maximum firing rate. A few cells were observed to receive presumably disynaptic inhibitory synaptic input following an action potential. In such cases, kinetics of APs later in the train were compromised and therefore excluded from analysis. Susceptibility to use-dependent change of the various AP kinetics was assessed by dividing the values of 5th-10th AP by the values of the 1st APs in a train, using APs with f_{inst} <20 Hz from datasets recorded at physiological temperature. The average across these normalized measures of AP change (excl AP udsr), was taken as a compound measure of AP stability.

Firing patterns

Firing patterns were analyzed using the inter-spike intervals (ISI) of trains of APs (7-13 spikes) evoked by 1s depolarizing current injections. Measures selected to capture distinct aspects of spike train regularity and temporal structure were: (1) Burst index, defined as the ratio of the last ISI to the first ISI, quantifies the degree of spike frequency adaptation within a train. (2) Local variation (LV), defined as: $LV = \frac{1}{n}\sum \left[\frac{3(ISI_i - ISI_{i+1})^2}{(ISI_i + ISI_{i+1})^2}\right]$, where the summation is over all pairs (i,j) of ISI in the spike train, and n is the total number of ISI pairs. This approach quantifies the irregularity of spike timing by measuring how much consecutive intervals vary relative to their sum, with higher values indicating greater variability. (3) Maximum instantaneous frequency ($f_{max.inst}$), calculated as the inverse of the smallest ISI (Hz), captures peak firing frequency within the train. (4) Maximum ISI ratio, defined as the ratio of the largest to smallest ISI, quantifies the range of temporal variability. (5) Early spike proportion was the fraction of action potentials occurring within the first 100 ms of stimulus onset, reflecting the temporal distribution of spiking activity.

Input-output features

Gain was defined as the slope of the linear portion of the *f-I* (frequency-current) relationship. Full *f-I* curves were fit using the Hill function: $F(I) = \frac{F_{max} \cdot I^n}{I_{50}^n + I^n}$, where F_{max} is maximum firing rate, F_{50} the current for half-maximum response, and n the Hill coefficient controlling curve steepness. Only neurons that were pushed to fire close to predicted maximum were included. Input range was defined as the current span between levels that produce 10-90% of F_{max}.

Subthreshold filter properties were assessed using a chirp current injection protocol that consisted of a constant amplitude sinusoidal current stimulus with linearly increasing frequency over time (0.5-15 Hz over 15-30 s). The impedance amplitude profile (ZAP) was computed by taking the ratio of the fast Fourier transform of the recorded voltage response to the fast Fourier transform of the injected current waveform. Resonant frequency was identified as the frequency corresponding to maximum impedance (Z_{max}) in the ZAP profile. The 3 dB bandwidth cutoff frequency was calculated as: $f_{cutoff} = \frac{1}{\sqrt{2}} \times Z_{max}$

Combining datasets

Mouse data was pooled with data from other publications after verifying that experimental methods and feature definitions were comparable. Membrane tau from one dataset[6] was excluded for being calculated from the discharging rather than charging phase of the hyperpolarizing voltage response. Some studies reported voltage sag as the percentage change between the minimum peak response and steady-state voltage deflection. These were converted to sag ratios using the formula: $sag\ ratio = \frac{1}{1-\frac{sag\%}{100}}$. In contrast to humans, mouse rheobase was defined in most studies as the minimum current required to trigger a single AP. Where available[1,2,4], raw data files were accessed to extract measures of action potential use-dependency and spike train regularity, which were not reported in the original publications.

The intracellular and extracellular solutions used in the mouse datasets were very similar (Table S4 & S5) and as a result, the liquid junction potential (LJP), which was not corrected for in any of the studies, was comparable (14-16.9 mV; Supplementary table 2). Two studies conducted experiments at room temperature[5,6]; since temperature can have a profound impact on firing behavior, these studies were excluded from analyses involving AP stability and spike train regularity. After dealing with the considerations above, mouse data was pooled. Some laboratory-specific variation remained, which was accounted for by including laboratory as a fixed effect in the mouse GLMMs (below and Table S3).

Human recordings were digitized at a range of sampling intervals, which may impact the precision with which fast events like APs are captured. To detect sampling frequency-related bias in action potential kinetics, we compared measurements from the same human neurons (n=150) recorded at high and low sampling frequencies using Bland-Altman analysis. Most AP features showed <5% difference in values between sampling regimes and measurements were therefore pooled, but AP upstroke and downstroke velocities showed systematic bias >10%. This was corrected by fitting a first and second-degree polynomial, respectively, to the high-vs-low sampled values, which was then used to correct the values derived from low frequency acquisition.

Generalised linear mixed model building workflow

GLM models for the developmental trajectories of physiological features were built using R statistical software (R Core Team, 2023) and the glmmTMB package[14] (v1.1.10). The t-family distribution was chosen for its robustness to minor deviations from normality that are common in electrophysiological data. Models were designed following a stepwise approach, starting with the simplest linear model and progressively adding complexity. The developmental trajectory was initially modeled as a linear age effect, then compared against natural spline fits with varying degrees of freedom. Models were compared using ANOVAs to guide the selection of the most parsimonious model that adequately captured the developmental trajectory. Then, fixed effects (soma depth, sex, laboratory) and random effects (subject ID) were systematically evaluated, with each addition tested alone or in combination against the previous best model. The last phase addressed heteroskedasticity by incorporating dispersion formulas to allow residual variance to change with age, testing both linear and spline-based dispersion models. Final models (Table S3) were evaluated using the DHARMa package model diagnostics[15]. For a subset of models, diagnostics showed minor deviations in the upper or lower residual quantiles, which was deemed acceptable given our focus on mean developmental trends and variance changes. This statistical approach enabled us to account for the hierarchical structure of our data, including non-independence of observations from the same subject, depth-dependent effects within the supragranular layers, and age-related changes in variance, all critical factors for accurate characterization of neuronal maturation trajectories.

GLMM mean predictions and confidence intervals were derived from a parametric bootstrap procedure, where 10,000 simulated datasets were generated from the fitted model parameters and re-fitted employing the University of Cape Town's ICTS High Performance Computing Cluster. From each fit, estimated marginal means (EMMs) were extracted using the sjPlot package. Layer-specific predictions were derived as partial effects by fixing cortical depth to representative values for each layer (L2: 400µm, L3A: 700µm, L3B: 1000µm, L3C: 1300µm). Similarly, female- or male-specific partial effects were obtained from models where biological sex was included. Variance predictions were computed by applying the model's dispersion formula (Table S3). Predictions were spline-interpolated across the age range, with mean and 95% confidence intervals calculated from the resulting distribution. Parametric bootstrapping provides more robust and accurate confidence intervals compared to direct model predictions, particularly for mixed-effects models like these with non-Gaussian distributions and heteroskedastic variance structures.

Epilepsy etiology

To ensure that our developmental findings reflected normal cortical maturation rather than epilepsy-related pathology, we assessed whether epilepsy etiology or seizure history influenced the neuronal properties and developmental trajectories we observed. To assess the potential effects of epilepsy etiology on cortical lamination, we fit GLMs to analyze cortical thickness and supragranular layer 2-3 thickness as functions of age and etiology groups ($thickness \sim age + etiology_group$; Table S1). Cortical thickness showed a significant age-related decrease consistent with previous MRI-based reports, but no significant differences between epilepsy etiologies (Fig. S1d). Supragranular layer 2-3 thickness remained stable across age and also showed no significant differences between epilepsy etiologies (Fig. S1e). These findings indicate that the diverse epilepsy etiologies in our sample did not affect cortical architecture, which is in line with the apparently normal lamination and appearance of neurons during live inspection of brain slices prior to recording.

The influence of epilepsy etiology and seizure history on neuronal physiological properties and their developmental trajectories was assessed by including these factors in the GLM models for each physiological feature. Patient etiologies were grouped into four broad categories: Developmental (FCD, HME, NDD), Hippocampal sclerosis (MTS), Structural (SVM, LGT), and Other/Unknown (non-lesional, unknown etiology). To address collinearity between epilepsy duration and age (older patients will tend to have longer epilepsy exposure), we calculated age-adjusted epilepsy residuals using the formula: residuals = YearsEpilepsy - f(age), where f(age) represents a natural spline fit of epilepsy duration on age. These residuals quantify seizure exposure independent of subject age. We then tested three models: (1) addition of etiology group as a categorical fixed effect, (2) addition of age-adjusted epilepsy residuals as a continuous predictor, and (3) inclusion of both epilepsy residuals and their interaction with age to test whether seizure sensitivity varies across development. Across all physiological features, these epilepsy factors showed no significant effects or model improvements (assessed with likelihood ratio tests), with one exception: etiology group had a small but significant effect on sag ratio ($\chi^2 = 10.7$, $p = 0.013$), driven by differences between the Hippocampal sclerosis and Other/Unknown groups (contrast estimate between pairs = 0.045, $p = 0.040$). Overall, epilepsy-related factors did not substantially influence the developmental trajectories of neuronal physiological properties, in line with earlier reports showing that the impact of patient disease history on neuronal physiology is minimal[8,16], but see[19].

Together, this analysis adds to the growing evidence that surgically resected tissue as used in the present study shows no measurable effects of patient disease history on cortical lamination[20], pathological marker expression[16,17], neuronal physiology[8,16,20], morphology[21], or gene transcription[16,18].

Variance components

Some features were log-transformed prior to fitting (Table S3). For display/interpretability purposes and for normalization of developmental trajectories (below), mean predictions of log-transformed variables were back-transformed to the original scale by exponentiation. Variance estimates were approximated on the original scale using the log-normal transformation formula $exp(2 * \mu) \times (exp(\sigma^2) - 1)$, where μ and σ^2 represent the predicted mean and variance on the log scale, respectively. To estimate within- and between-subject variance components across age categories, we again used parametric bootstrap simulations from the final GLM models for each feature. Here (and henceforth below), simulations were generated with soma depth fixed at 750 µm (approx. L3A and close to mean depth of our sample), to eliminate variability due to differential depth sampling. For each replicate, variance components and intraclass correlation coefficients ($ICC = \frac{\sigma^2_{between}}{\sigma^2_{between}+\sigma^2_{within}}$) were calculated per age category. Pairwise differences in variance components between age categories were considered significant if Bonferroni-adjusted confidence intervals from the bootstrap distributions excluded zero. Age categories were defined as infancy (0-2), childhood (2-12), adolescence (12-20), and adulthood (>20).

Maturation peaks

The age of reaching adult maturity was estimated using the bootstrap replicates for each physiological feature that exhibited significant age-dependent change. For each replicate, adult 'peak' age was defined as the first time beyond the juvenile period (>12 years human, >12 days mouse) where developmental change slowed to <5% of the maximum rate of change (Fig. S2c). For some non-monotonic trajectories, the identified plateau value was inconsistent with the overall developmental direction (e.g. in case of saddle points, where trajectories increased overall but showed local minima, or vice versa). In such cases, only plateau values >20 were retained. Adult maturity age was defined as the median of the resulting adult peak age distribution. The associated uncertainty was quantified by the IQR and 2.5-97.5% percentiles, which reflect how parameter estimation uncertainty in the fitted model translates into uncertainty about maturation timing.

The average developmental trajectory of each feature was normalized to a 0-1 scale based on the parameter's value at the youngest age sampled and the value at its identified adult age: $N(t) = \frac{P(t)-P_0}{P_{adult}-P_0}$ for increasing trajectories and $N(t) = \frac{P_0-P(t)}{P_0-P_{adult}}$ for decreasing trajectories, where $P(t)$ is the parameter value at age t, P_0 is the initial/infant value, and P_{adult} is the adult value. For cross-species comparison via dynamic time warping analysis (below), mouse trajectories were normalized over an equivalent neurodevelopmental window: mouse P_0 was redefined as the parameter value at postnatal day P6.3, the age when mouse brain volume reaches 57% of adult volume, matching the relative brain maturation stage of our youngest human subject (0.91 years).

Brain development curves

We obtained postnatal brain development curves for both species from published literature that characterized the postnatal growth of human[22] and mouse[23] brain structures using MRI. We used cerebrum volume as our reference measure, using the publicly available human model from Bethlehem et al. (2022). Mouse brain volume trajectories were modeled using logistic growth curves[23]: $V(t) = \frac{a}{1+exp\left(-\frac{(t+18.5)-x_0}{b}\right)}$, where t is postnatal age in days. Mouse cerebral volume was calculated by subtracting cerebellar from total brain volume, obtained using the parameters for total brain (a = 429, x_0 = 24.0, b = 4.2) and cerebellum volume growth (a = 48, x_0 = 27.0, b = 3.6)[23] . For the dynamic time warping analysis procedures below, brain growth curves were normalized as described for physiological maturation trajectories above.

Dynamic time warping analysis

For cross-species comparison of brain anatomical and neuron physiological maturation rates, we performed dynamic time warping (DTW) analysis on normalized developmental trajectories for human and mouse. The DTW algorithm constructs a pairwise distance matrix between all time points of the two developmental series (days for mouse, years for humans), then identifies the optimal warping path that minimizes the cumulative distance between aligned ages. Both species exhibited developmental trajectories with similar shapes typical of biological maturation processes, resulting in nearly linear optimal warping paths. This linear relationship indicates that relative maturation rates between species can be effectively captured by a single scaling factor, the slope of the warping path, which quantifies the temporal scaling of human and mouse development. Only features that had a significant age effect in the GLM models for both species were included in this analysis. For brain development, the trajectories spanned from birth to when 99% brain volume was reached in both species. For physiological features, trajectories were normalized over an equivalent brain growth window (57-99%, see above). Developmental scaling coefficients were derived from the ratio of physiological to anatomical scale factors (physiology/brain growth), capturing the extent to which physiological and anatomical maturation are proportionally scaled across species.

Allometry

To explore allometric relationships between maturation of physiological features and brain volume growth, we took from each bootstrap simulated sample (above) the portion that covered the growth phase, from .91 yrs in human and P2 in mouse, up to 99.9% brain volume or up to adult peak age, whichever came first. Age was then transformed to expected brain volume using the brain growth curves described above. Simulated values and brain volumes were then log-transformed and the slope of the linear fit was obtained, representing the allometric scaling exponent α in the power law function $y = bx^{\alpha}$.

Reported α values in the text and figures are the median of the resulting distribution of values. Statistical significance of allometric scaling differences between species was assessed using a bootstrap difference distribution approach. For each variable, 10,000 difference samples were generated by randomly sampling one α value from each species' distribution and calculating the difference. Statistical significance was determined when the 95% confidence interval of the difference distribution did not include zero. P-values were calculated as twice the proportion of difference samples on the opposite side of zero from the median difference, representing a two-tailed test.

Gaussian mixture modeling

Gaussian mixture modeling (GMM) was employed to identify distinct developmental states or cell types within the neuronal population. GMM assumes that data points arise from a mixture of multiple Gaussian distributions, making it particularly suitable for capturing the potentially overlapping and continuous nature of neuronal developmental trajectories. The analysis included 403 neuronal observations with 25 electrophysiological features, which included all sub- and suprathreshold properties, AP kinetics and stability measures mentioned above, with the addition of a set of spike-train regularity measures. To minimize potential confounds from recording depth, neurons were restricted to those with soma depths ≤1200 μm. Only complete cases without missing values were retained for analysis. Variables with skewed distributions were log-transformed and all features were subsequently standardized to z-scores to ensure equal weighting across variables with different scales and units.

GMM clustering was performed using the MClust package (version 6.1.1)[24]. Models with diagonal covariance matrices allowing varying volume and shape (VVI specification) were tested across 3-10 components. The optimal number of components was determined by identifying the model with the minimum absolute Bayesian Information Criterion (BIC) score, which was 7. To ensure robust and reproducible clustering, Jaccard similarity was used to assess cluster stability. For each candidate model, 100 subsamples of 90% of the data were generated. GMM was fit to each subsample, and the Jaccard index (the ratio of intersection to union of cluster memberships) was calculated between the full dataset clusters and their best-matching subsample counterparts. The final model was selected by progressively reducing the number of clusters until all clusters achieved mean Jaccard similarity >0.5, which was the case with 5 clusters. Cluster robustness was then further validated using a co-clustering analysis. Across 500 bootstrap iterations (90% subsampling), the frequency with which each pair of neurons was assigned to the same cluster was used to generate the co-clustering probability matrix.

To model the continuous progression of neuronal electrophysiological properties during development, we employed trajectory inference analysis using the Slingshot package[25]. This orders cells along pseudotime, a continuous variable representing each cell's relative position along an inferred developmental trajectory, based on their phenotypic similarities in the high-dimensional feature space. Based on the GMM clustering results we specified cluster 1 (containing the youngest neurons) as the starting point and clusters 4 and 5 (predominantly adult neurons) as endpoints. This resulted in two putative maturation paths through the two-dimensional UMAP embedding from infancy to adulthood.

PERMANOVA analysis

To test whether electrophysiological profiles differed significantly between age categories, we performed permutational multivariate analysis of variance (PERMANOVA) using adonis2 from the vegan package[26]. Euclidean distances were calculated from the same feature matrix used for GMM above. The model included soma depth as a covariate and age category as the main factor of interest (physiological_distances ~ cell_depth + age_group), with 999 permutations and sequential testing by terms. Post-hoc pairwise comparisons were done between all age categories and with Bonferroni corrected p-values. To confirm robustness against multicollinearity among variables, we repeated the analysis using PCA-transformed data (11 components explaining >1% variance), which yielded similar results (PERMANOVA, $F_{3,398} = 38.8$, $p < 0.001$, $R^2_{age_group} = 0.22$, $R^2_{depth} = 0.05$; all post hoc pairwise comparisons significant, $p < 0.01$).

References

1. Kroon, T., van Hugte, E., van Linge, L., Mansvelder, H. D. & Meredith, R. M. Early postnatal development of pyramidal neurons across layers of the mouse medial prefrontal cortex. *Sci. Rep.* **9**, 5037 (2019).
2. Ciganok-hückels, N., Jehasse, K. & Kampa, B. M. Postnatal development of electrophysiological and morphological properties in layer 2 / 3 and layer 5. 1–10 (2022).
3. Oswald, A.-M. M. & Reyes, A. D. Maturation of Intrinsic and Synaptic Properties of Layer 2/3 Pyramidal Neurons in Mouse Auditory Cortex. *J. Neurophysiol.* **99**, 2998–3008 (2008).
4. Gouwens, N. W. *et al.* Classification of electrophysiological and morphological neuron types in the mouse visual cortex. *Nat. Neurosci.* **22**, 1182–1195 (2019).
5. Scala, F. *et al.* Phenotypic variation of transcriptomic cell types in mouse motor cortex. *Nature* **598**, 144–150 (2021).
6. Weiler, S. *et al.* Functional and structural features of L2/3 pyramidal cells continuously covary with pial depth in mouse visual cortex. *Cereb. Cortex* 1–19 (2022) doi:10.1093/cercor/bhac303.
7. Testa-Silva, G. *et al.* Human synapses show a wide temporal window for spike-timing-dependent plasticity. *Front. Synaptic Neurosci.* (2010) doi:10.3389/fnsyn.2010.00012.
8. Verhoog, M. B. *et al.* Mechanisms underlying the rules for associative plasticity at adult human neocortical synapses. *J. Neurosci. Off. J. Soc. Neurosci.* **33**, 17197–208 (2013).
9. Horikawa, K. & Armstrong, W. E. E. A versatile means of intracellular labeling: injection of biocytin and its detection with avidin conjugates. *J. Neurosci. Methods* **25**, 1–11 (1988).
10. Schindelin, J. *et al.* Fiji: an open-source platform for biological-image analysis. *Nat. Methods* **9**, 676–682 (2012).

11. Kalmbach, B. E. *et al.* h-Channels Contribute to Divergent Intrinsic Membrane Properties of Supragranular Pyramidal Neurons in Human versus Mouse Cerebral Cortex. *Neuron* **100**, 1194-1208.e5 (2018).
12. Lapique, L. Researches quantatives sur l'excitation electrique des nerfs traitee comme une polarization. *J. Physiol. Pathol. Genet.* **9**, 620–635 (1907).
13. Weiss, G. Sur la possibilite de rendre comparables entre eux les appareils servant a l'excitation electrique. *Arch Ital Biol* **35**, 413 (1901).
14. Brooks, M., E. *et al.* glmmTMB Balances Speed and Flexibility Among Packages for Zero-inflated Generalized Linear Mixed Modeling. *R J.* **9**, 378 (2017).
15. Hartig, F. DHARMa: Residual Diagnostics for Hierarchical (Multi-Level / Mixed) Regression Models. (2024).
16. Berg, J. *et al.* Human neocortical expansion involves glutamatergic neuron diversification. *Nature* **598**, 151–158 (2021).
17. Pegasiou, C. M. *et al.* Age-Dependent Changes in Synaptic NMDA Receptor Composition in Adult Human Cortical Neurons. *Cereb. Cortex* 1–11 (2020) doi:10.1093/cercor/bhaa052.
18. Hodge, R. D. *et al.* Conserved cell types with divergent features in human versus mouse cortex. *Nature* **573**, (2019).
19. Kushner, J. K. *et al.* Characterizing the Diversity of Layer 2/3 Human Neocortical Neurons in Pediatric Epilepsy. *eneuro* **12**, ENEURO.0247-24.2025 (2025).
20. Heyer, D. B. *et al.* Verbal and General IQ Associate with Supragranular Layer Thickness and Cell Properties of the Left Temporal Cortex. *Cereb. Cortex* **32**, 1–15 (2022).
21. Mohan, H. *et al.* Dendritic and Axonal Architecture of Individual Pyramidal Neurons across Layers of Adult Human Neocortex. *Cereb. Cortex* **25**, 4839–4853 (2015).
22. Bethlehem, R. A. I. *et al.* Brain charts for the human lifespan. *Nature* **604**, 525–533 (2022).
23. Chuang, N. *et al.* An MRI-based atlas and database of the developing mouse brain. *NeuroImage* **54**, 80–89 (2011).
24. Scrucca, L., Fraley, C., Murphy, T. & Raftery, A. Model-Based Clustering, Classification, and Density Estimation Using mclust in R. (2023).
25. Street, K. *et al.* Slingshot: cell lineage and pseudotime inference for single-cell transcriptomics. *BMC Genomics* **19**, (2018).
26. Oksanen, J. *et al.* vegan: Community Ecology Package. The R Foundation https://doi.org/10.32614/cran.package.vegan (2001).

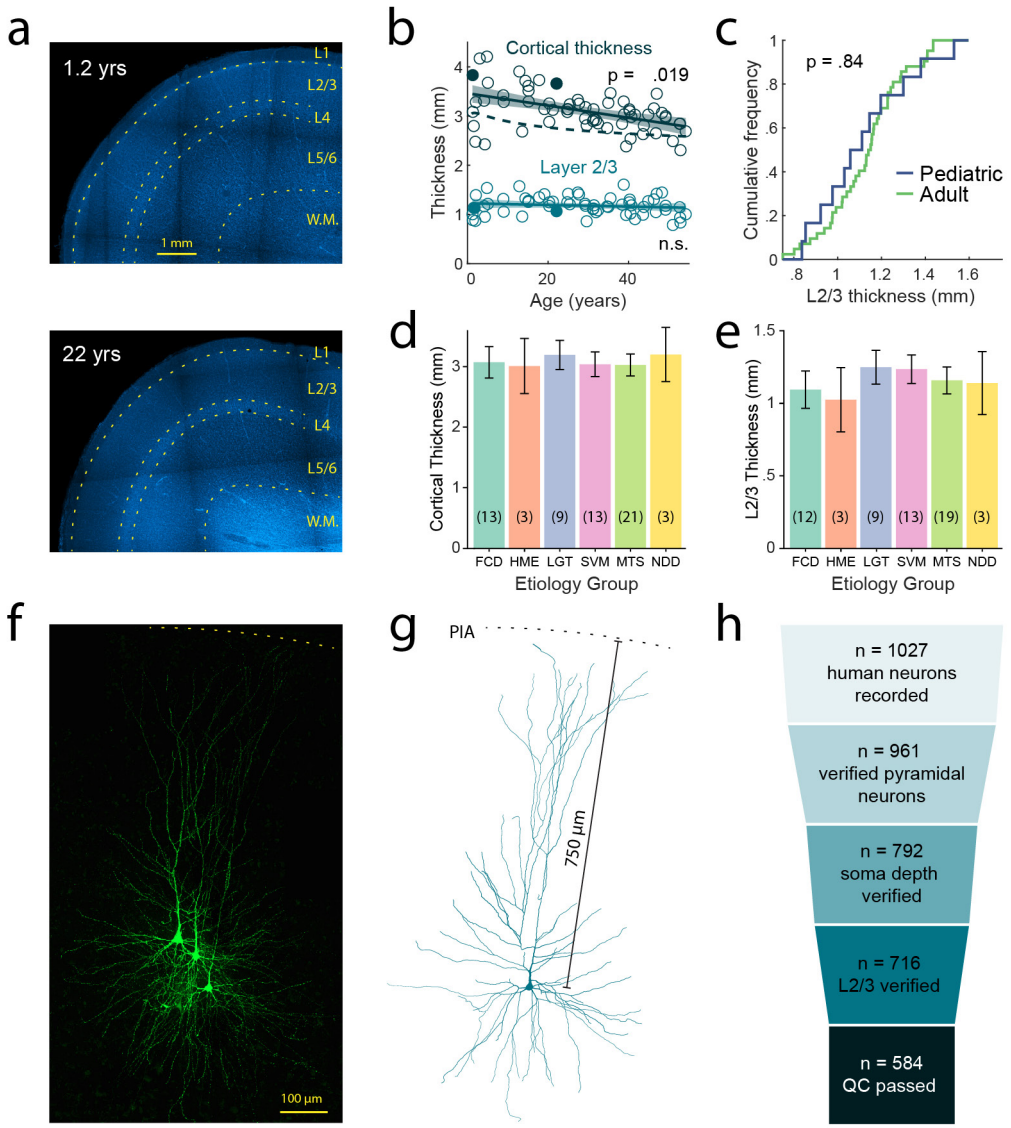

Figure S1. Histology and cell selection. a, Example images of DAPI stained cortical slices, used to estimate layer boundaries (yellow dashed) and cortical thickness. Note fainter white matter in the infant due to lower degree of myelination. **b**, Cortical thickness and L2/3 thickness estimates vs age. Cortical thickness (CT) decreases mildly with age (-12.4 µm/year; $p < 0.001$, $R^2 = 0.24$, 64 subjects), in line with earlier reported age-dependent cortical thinning (dashed line: MRI-based CT estimate from Bethlehem et al., 2022), in contrast to supragranular layers 2/3 (-1.6 µm/year; $p = 0.28$, $R^2 = 0.003$, 61 subjects). Filled circles correspond to examples in a. c, Cumulative frequency plots of pediatric (≤12 yrs) and adult (≥20 yrs) layer 2/3 thickness. No difference was observed in the distribution between age groups (Kolmogorov-Smirnov test; $p = 0.837$, $n_{ped} = 12$, $n_{adult} = 42$). **d**, Cortical thickness for different epilepsy etiologies. Values represent age-corrected group means ± 95% confidence intervals. No significant differences were observed between epilepsy etiologies (all pairwise Tukey-adjusted comparisons $p > 0.84$). FCD: focal cortical dysplasia, HME: hemimegalencaphaly, LGT: low-grade tumors, SVM: structural/vascular malformations, MTS: mesial temporal sclerosis, NDD: neurodevelopmental disorders (Table S1). **e**, Same as d for supragranular layer 2-3 thickness. No significant differences were observed between epilepsy etiologies (all pairwise comparisons $p > 0.52$). **f**, Example image of neuronal morphology of recorded neurons, visualized by Alexa488-streptavidin stain of biocytin-filled neurons. **g**, 3D reconstruction of right-most cell in **f**, showing measurement of soma depth along apical dendrite. **h**, Funnel diagram presenting sequential selection criteria for neuron inclusion in the study.

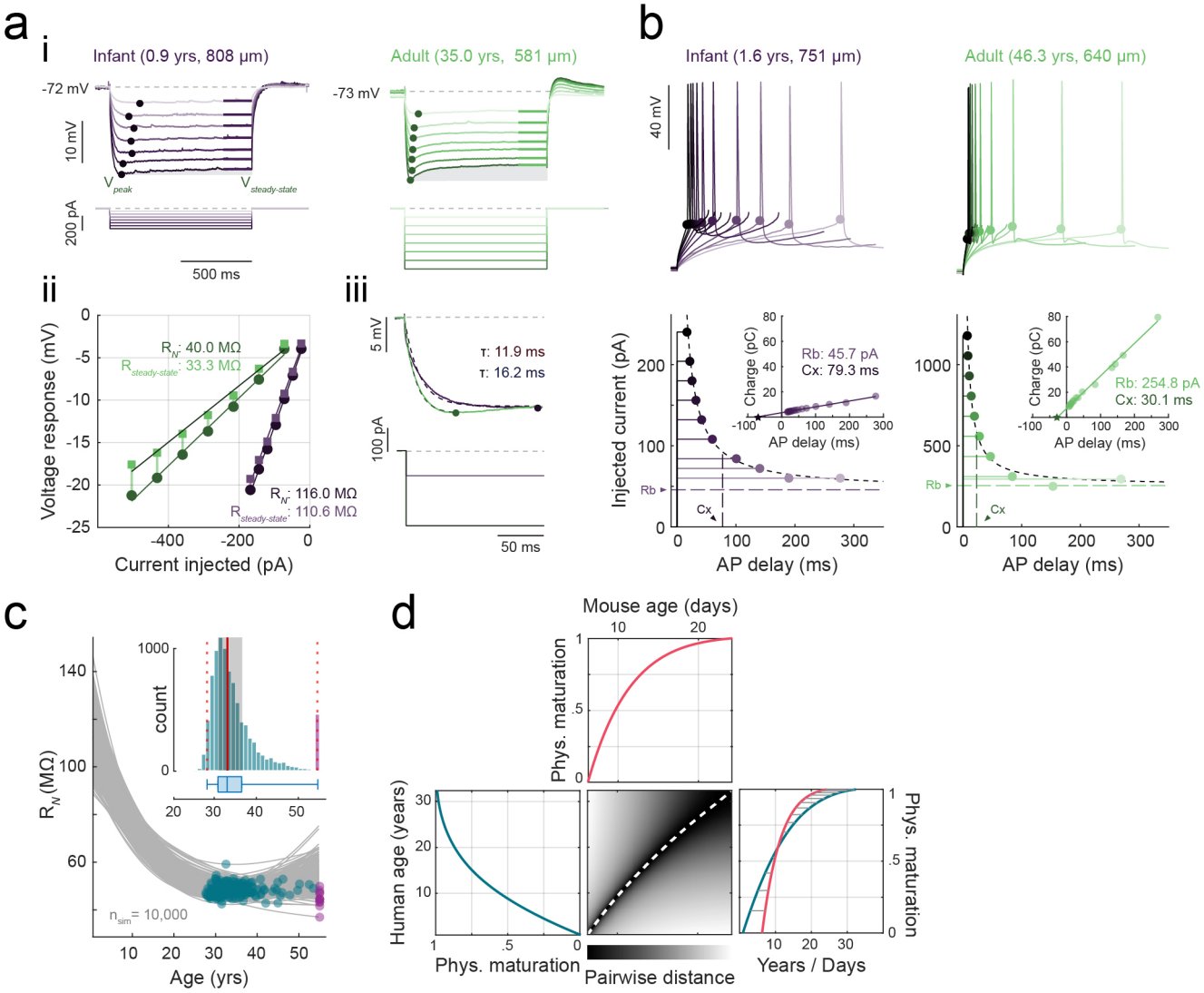

Figure S2. Feature extraction. a, Subthreshold feature extraction. i) Voltage responses (top) to hyperpolarizing current pulses (bottom) from infant and adult example neurons. Peak voltage and steady state voltage deflections marked by dots and horizontal bars, resp. Grey shaded area shows voltage change due to HCN-channel activation (I_h), which is notably larger in the adult neurons, resulting in more prominent voltage 'sag'. ii) *I-V* graph of the peak and steady-state voltage deflections for both neurons. Slope of the linear fit to V_{peak} values gives the neural resistance R_N. Sag ratio was defined as the ratio $R_N/R_{steady\text{-}state}$. iii) Examples of single exponential fits from start to peak voltage deflection, yielding the membrane time constant (τ) of the cell. **b**, Rheobase () and chronaxie () were estimated using the relationship between current amplitude and delay to the first AP. Top traces show AP delay (time from onset of current pulse to threshold), which is related to stimulus intensity (bottom panel) following Lapicque's equation , which produces a hyperbolic curve with an asymptotic approach to (bottom panel, dashed fit). When transformed to charge-duration (inset), this yields a linear relationship where threshold charge . This approach allowed robust estimation of rheobase (slope) and chronaxie (-x intercept, star) for cells with varying stimulus durations or with a limited number of suprathreshold responses available. **c**, Peak maturation age for physiological features was estimated using 10,000 bootstrap replicate samples from the GLM models and fit (grey lines, showing subset of 250 fits to human R_N replicates), and for each the adult peak age (blue dots) was determined. The distribution of peak values (inset) yielded the median peak age (red line) and provided measures of prediction accuracy in the form of IQR (shaded) and 2.5-97.5% percentiles (dashed), summarized in box plot below. Purple dots mark fits where no plateau value was reached within sampled age range. **d**, Dynamic time warping analysis of developmental trajectories between human and mouse. For each species, developmental trajectories were min-max normalized over the same brain growth period, shown here for R_N. Central heatmap displays pairwise distance matrix with optimal warping path (white dashed line) aligning species' development across temporal scales. The right panel shows maturation curves for both species overlaid, with a subset of the DTW matched time points linked in grey.

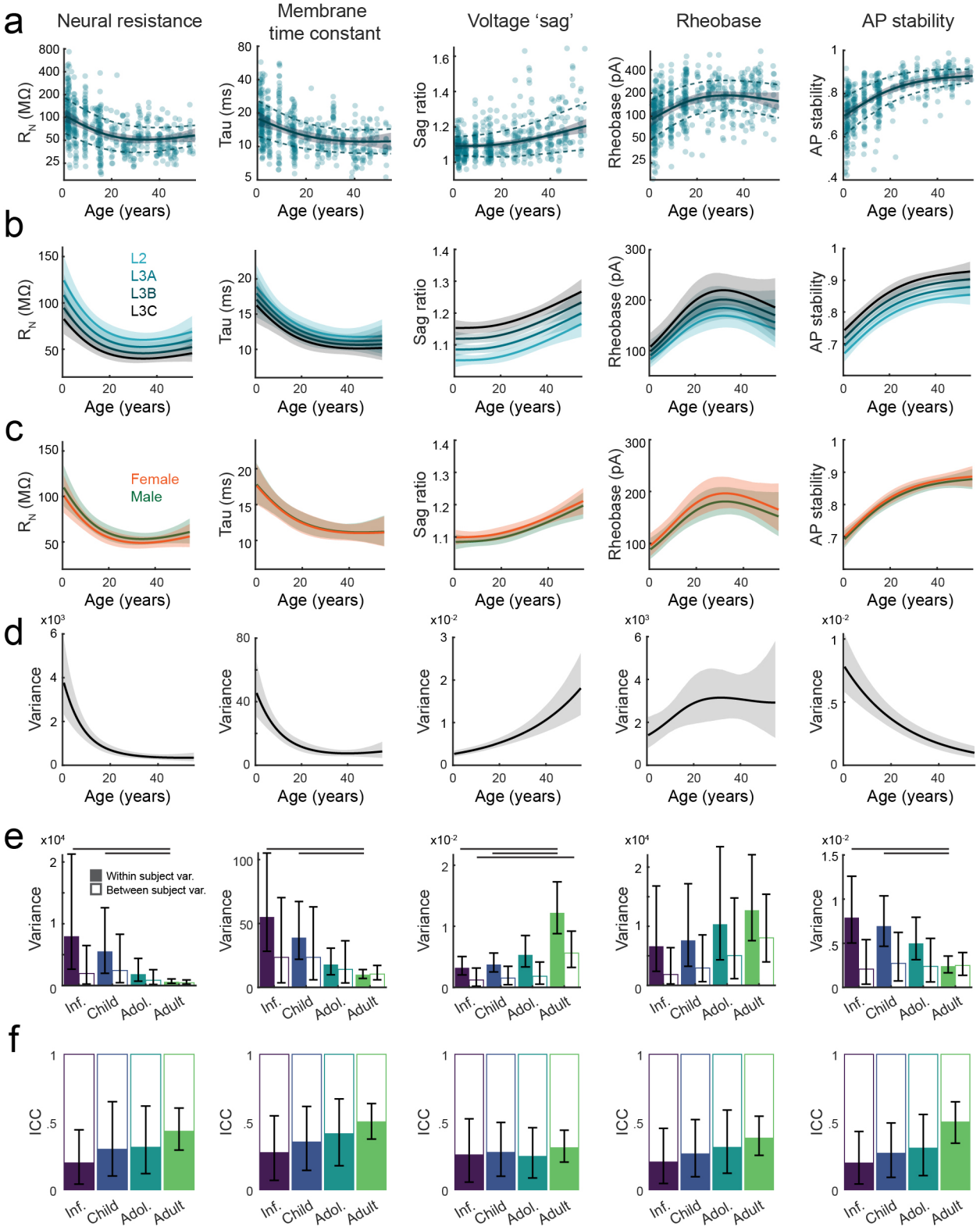

Figure S3. Generalized linear mixed models of physiological developmental trajectories. a, GLM fits for neural properties presented in Fig. 1, with the same scale as used for fitting. Each point represents a single neuron measurement. GLMM-predicted mean trajectory with 95% confidence intervals shown by solid line and shading. **b**, Developmental trajectories for the 4 supragranular pyramidal cell sublayers (L2, L3A, L3B, L3C). Soma depth was a significant fixed effect in all GLM models. **c**, Developmental trajectories by biological sex. Including sex as a fixed effect did not significantly improve model fit for any of the features tested. **d-f** variance measures for the same properties as **a-c**. **d**, Age-related changes in variance. Most showed significant heteroskedasticity with age, requiring inclusion of a variance model component in the GLMMs. Variance estimates shown as mean ± 95% confidence intervals from parametric bootstrap replicates. **e**, Analysis of within- vs between- subject variance. Mean ± 95% confidence intervals of within and between- subject variance for broad age categories. Age-related changes in variance seem primarily driven by changes in within-subject variability. **f**, Intraclass correlation coefficients (ICC) for each developmental stage. Values shown as mean ± 95% confidence intervals. No significant differences were observed between age categories ($p > 0.05$), indicating that the proportion of variance attributable to inter-subject differences remains consistent across development.

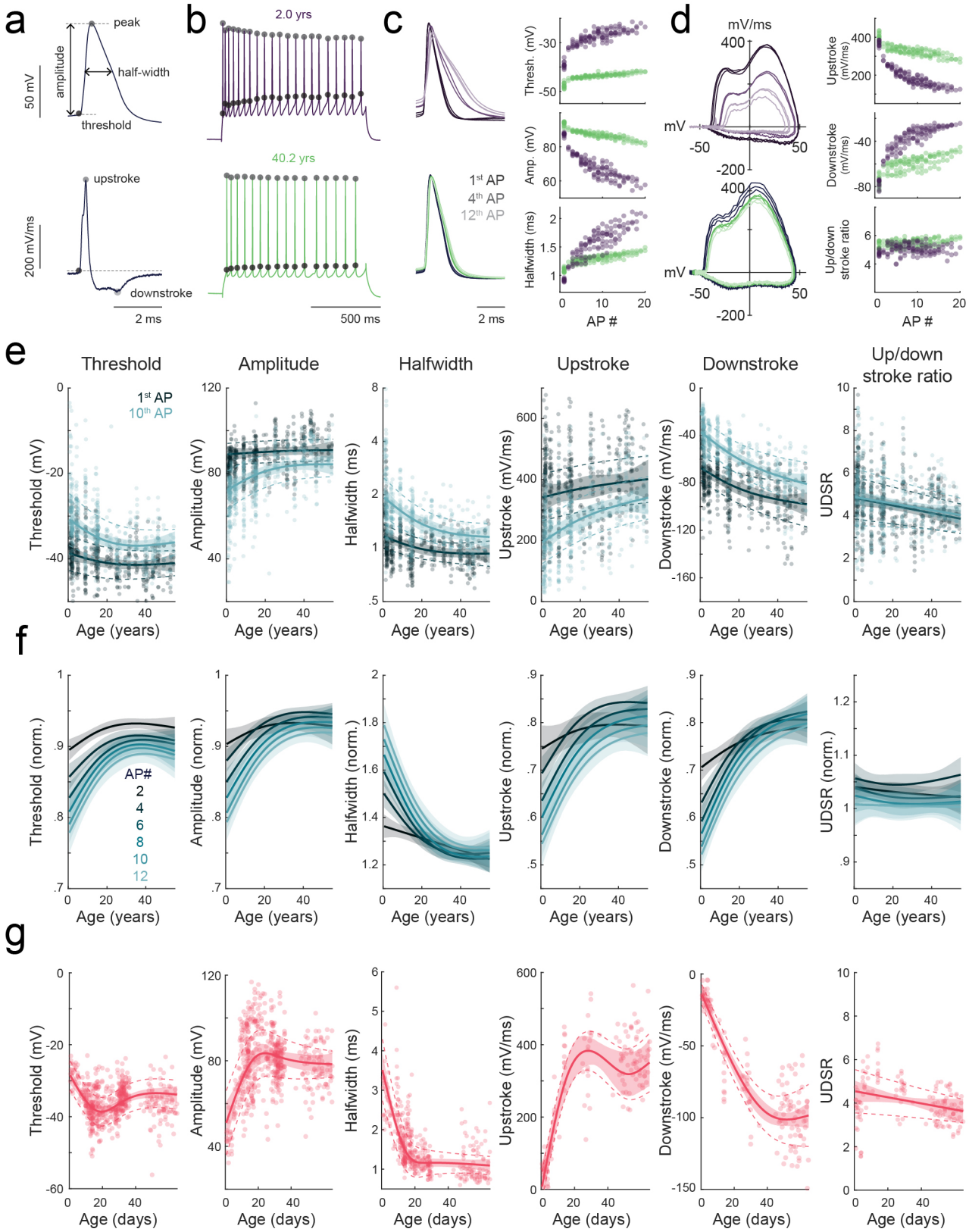

Figure S4. Action potential kinetics. a, Example action potential waveform (top) and derivative (bottom) showing extraction of kinetic features. Threshold was determined as the point where the derivative last crossed 10 mV/ms. **b**, AP trains recorded from infant (top) and adult (bottom) example neurons, dots marking AP threshold and peaks. Note the progressive increase in threshold and decrease in peak voltage during firing in the infant neuron, in contrast to the adult. **c**, Left: Waveform overlay of APs at different positions in the train. Right: kinetic features of 100 APs from same example neurons, plotted versus AP number in the train. Note the pronounced use-dependent change in infant cell AP kinetics, as opposed to the stable adult APs. **d**, As **c**, for AP phase planes and measures relating to AP rise and fall speed. **e**, GLMM fits to AP kinetics of the 1st and 10th AP. **f**, GLMM fits to AP kinetics normalized to the 1st AP. Note the greater impact of AP number on kinetics in young individuals compared to adults. **h**, GLMM fits to mouse 1st AP kinetics.

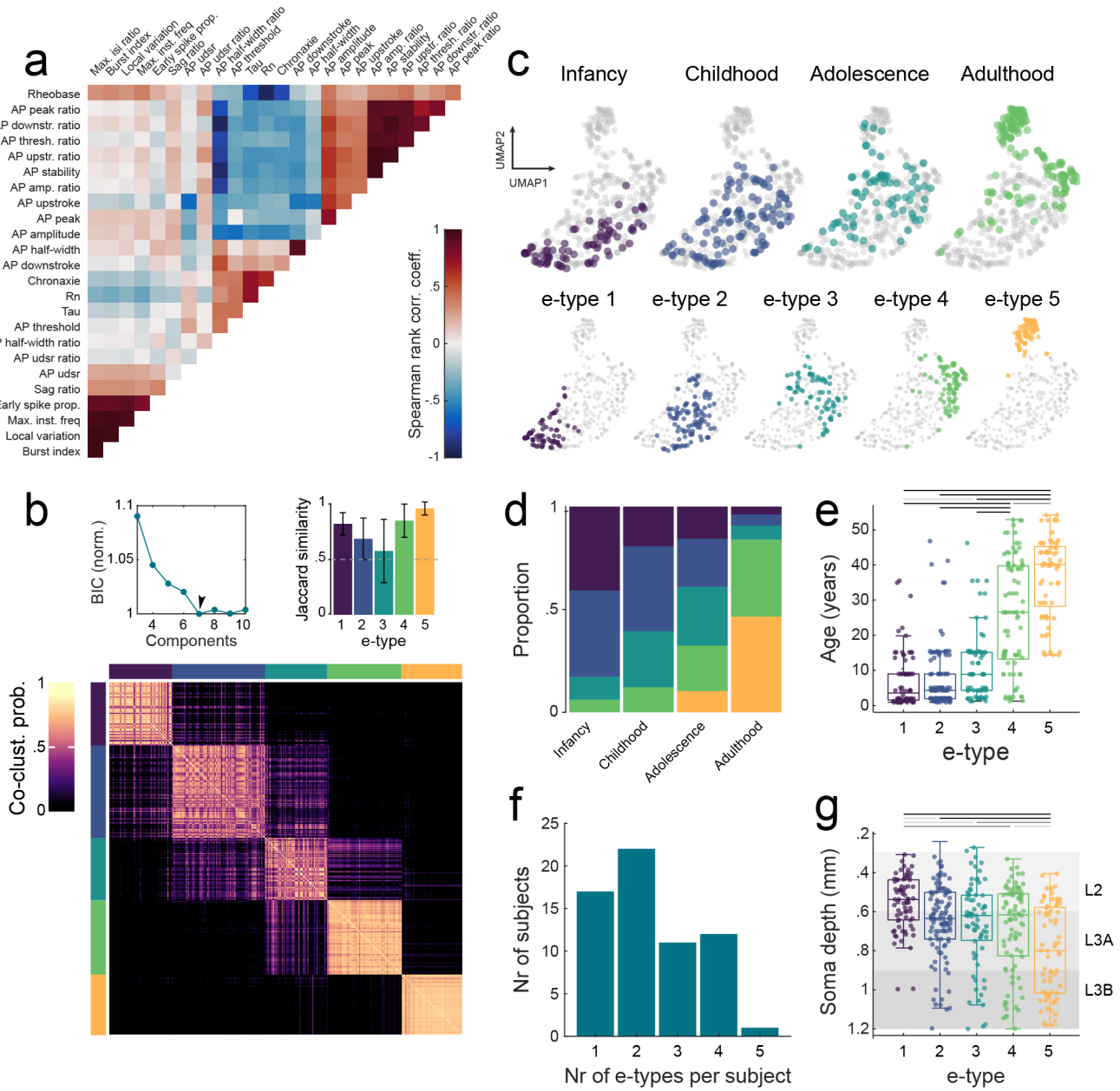

Figure S5. Gaussian mixture modelling for the identification of developmental e-types. a, Cross-correlation matrix of electrophysiological features used in Gaussian mixture modeling. Heatmap displays Spearman rank correlation coefficients between all pairs of z-score normalized electrophysiological parameters. **b**, Model selection for Gaussian mixture modeling of electrophysiological data. Top left: Normalized Bayesian Information Criterion (BIC) scores across different numbers of mixture components, showing optimal fit at 7 components (lowest absolute BIC value, arrowhead). Top right: Jaccard similarity analysis results for the final 5-component solution, where all clusters (e-types) exceeded the 50% Jaccard similarity threshold for stable clustering. Bottom: Co-clustering probability matrix, showing the high probability that pairs of data points within the 5 e-types are assigned to the same cluster across 500 model runs. **c**, Two-dimensional UMAP of electrophysiological feature space colored by broad developmental stage (top), revealing developmental progression. Bottom shows same UMAP, with neurons colored by their assigned electrophysiological type (e-type 1-5), demonstrating how the five distinct e-types are distributed along a similar developmental trajectory. **d**, Stacked bar chart showing e-type composition of different developmental age categories, which differed significantly ($\chi^2(12, n = 403) = 230.67$, $p < 0.001$). **e**, Age distribution across e-types. Box plots show significant age differences between e-types (Kruskal-Wallis $H(4) = 187.98$, $p < 0.001$). Bars indicate significant pairwise comparisons ($p < 0.05$, Tukey HSD post hoc tests). **f**, Histogram showing the distribution of how many e-types are found per subject in the dataset. **g**, Depth distribution across e-types. Box plots show significant differences in somatic depth between e-types (Kruskal-Wallis $H(4) = 41.647$, $p < 0.001$). Bars indicate significant pairwise comparisons ($p < 0.05$, Tukey HSD post hoc tests).

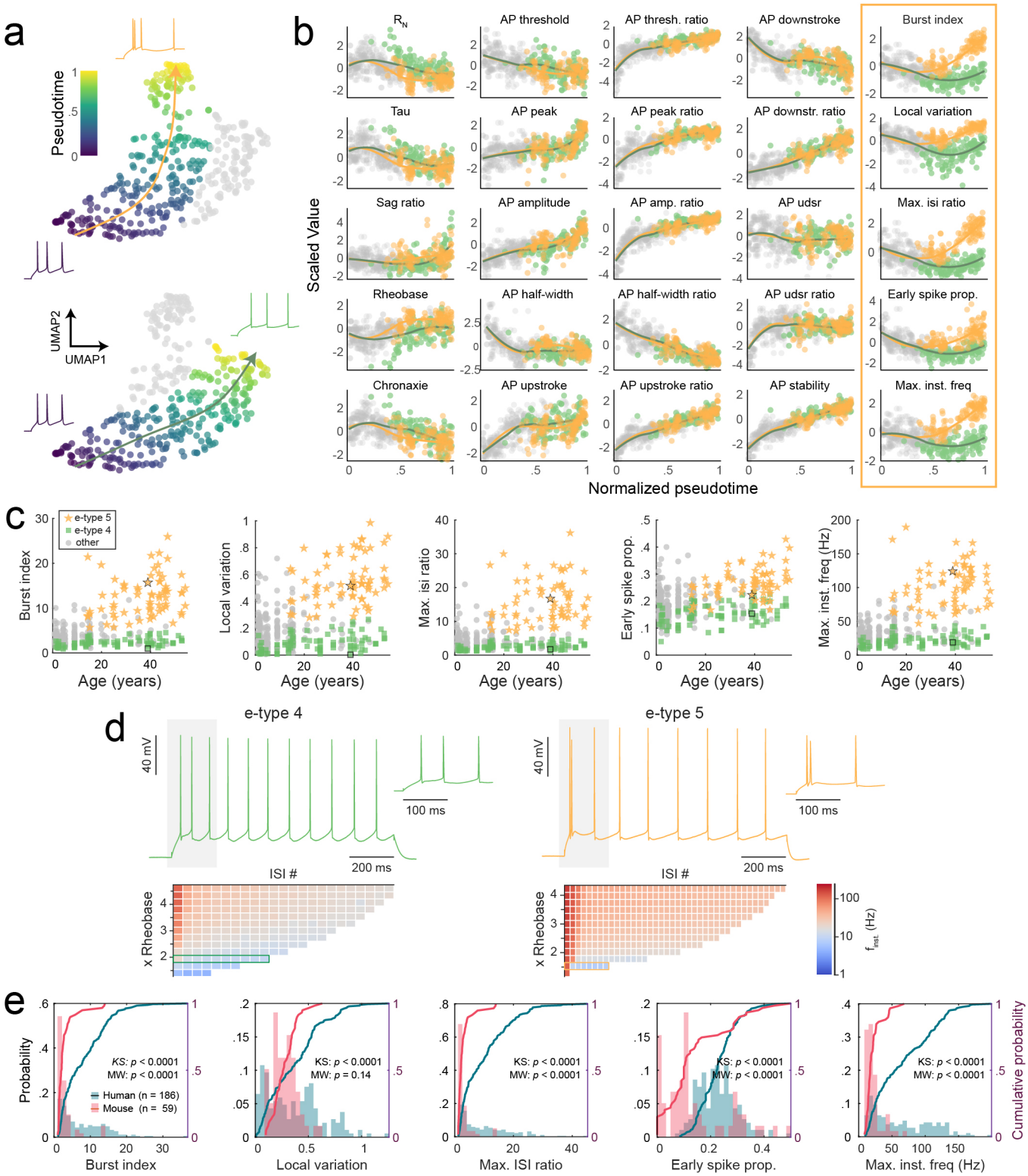

Figure S6. Late emergence of the adult burst firing phenotype. a, Slingshot trajectory analysis mapping maturation along two putative maturation paths through UMAP space. Neurons colored by pseudotime, voltage traces show examples of firing patterns at start and endpoint of each trajectory. **b**, Parameter z-scores plotted against normalized pseudotime for both lineages (orange: lineage 1, green: lineage 2, grey: shared) with overlaid LOESS curves. Both lineages share common early developmental features but diverge in measures of firing regularity and frequency (box). **c**, Age-related changes in firing regularity metrics. Note the late divergence of the dominant adult e-types. Outlined datapoints correspond to examples in **d**. **d**, Example recordings of e-type 4 and e-type 5 firing behavior. Top traces show how e-type 4 neurons fire highly regular trains of APs, whereas e-type 5 neurons commence firing with a burst of 2 or more APs (insets). Below: Instantaneous firing frequency for each AP in train evoked with progressively increasing stimulus intensity (multiples of rheobase). Row corresponding to trace above is boxed. Note how e-type 5 neuron initiates firing at all stimulus intensities with a >100Hz burst, whereas e-type 4 only reaches such rates when stimulated >4x Rheobase. **e**, Adult human versus mouse firing properties. Adult human pyramidal neurons exhibit a wider variety of firing phenotypes, ranging from very regular to strong burst firing. The latter appears absent in mouse supragranular layers.

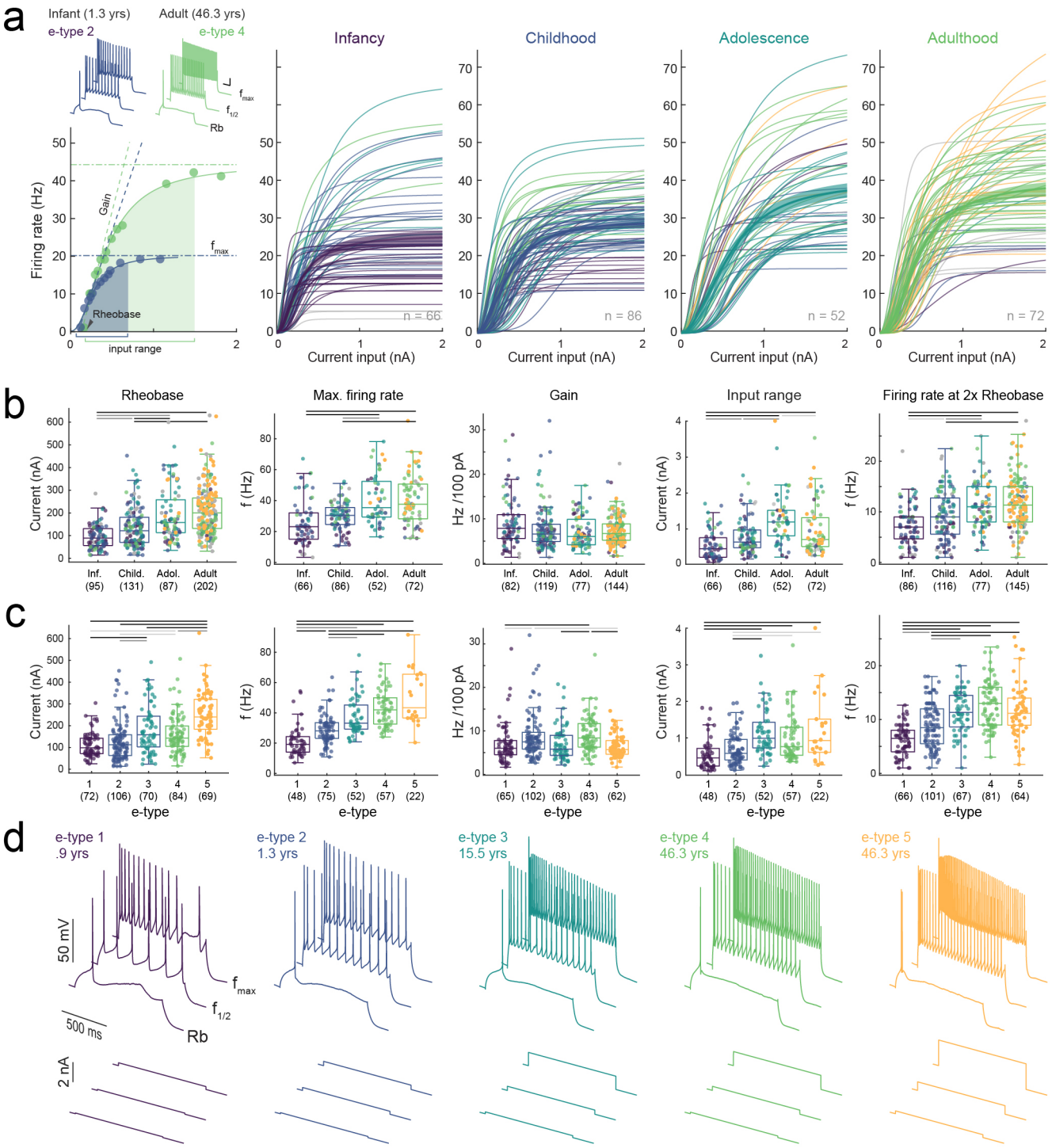

Figure S7. IO properties. a, Input-output relationships across broad age categories. Left: *f-I* (firing frequency vs input current) relationship plot demonstrates how input-output features were extracted. Right: *f-I* curve fits for different age categories, colored by e-type. Grey = no e-type assigned. **b**, Box plots showing distribution of key input-output features across age categories. All features except gain showed significant differences between age categories (Kruskal-Wallice test, $p < 0.05$,). **c**, Same as **b** for e-types. All features showed significant differences between e-types (Kruskal-Wallice test, $p < 0.05$). **d**, Enlarged examples of the AP firing patterns shown in Fig. 3g, with associated current injections (bottom) for the 5 e-types.

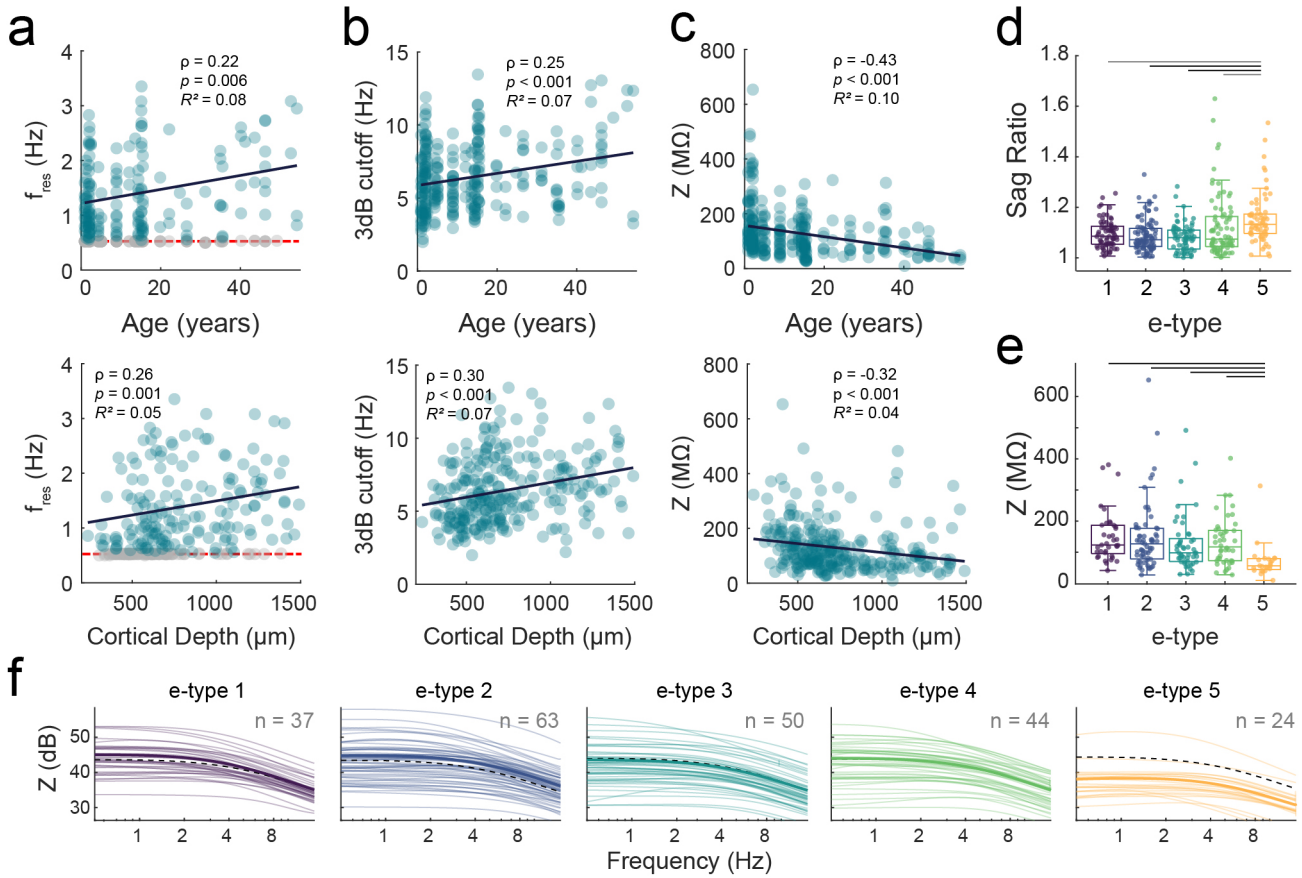

Figure S8. Subthreshold filtering properties. a, Resonant frequency significantly increased with age (top) and soma depth (bottom). Grey dots mark resonant frequencies at the lowest frequency tested (0.5 Hz, red dash). **b**, As **a**, for 3Db cutoff frequency, which significantly increased with age and soma depth. **c**, As **a**, for average impedance below cutoff frequency. Impedance decreased significantly with age and soma depth. **d**, Box plot showing sag ratio was significantly greater in e-type 5 neurons compared to all other e-types (Kruskal-Wallice test, $p < 0.05$). **e**, Box plot showing impedance was significantly smaller in e-type 5 neurons compared to all other e-types (Kruskal-Wallice test, $p < 0.05$). **f**, Bode magnitude plots showing impedance vs frequency (log scale). Impedance reported in dB (re 1 MΩ:) to better visualize the full range of response profiles (thin lines: individual neurons, thick lines: e-type mean, dashed line: population average). Note markedly lower impedance of e-type 5 across the entire sampled frequency range.

Table S1 - Donor sample

Subject	Sex	Age (yrs)	Hemisphere	Cortical area	Epilepsy yrs	Etiology	# Cells
1	Male	0.9	Left	Temporal	0.9	HME	17
2	Male	1.2	Right	Temporal	1.2	HME	13
3	Male	1.3	Left	Temporal	1.3	FCD	9
4	Female	1.6	Left	Temporal	1.4	FCD	23
5	Male	2.0	Right	Temporal	1.9	FCD	27
6	Female	2.0	Left	Temporal		LGT	12
7	Female	2.1	Left	Temporal	2.1	HME	21
8	Female	2.5	Right	Temporal	2.3	NA	10
9	Female	3.0	Left	Temporal	3.0	FCD	4
10	Male	4.1	Left	Temporal	3.3	FCD	7
11	Male	4.3	Right	Temporal	2.2	SVM	1
12	Male	4.3	Right	Temporal	1.6	FCD	26
13	Female	4.8	Left	Temporal	2.4	NDD	2
14	Female	5.1	Right	Temporal	4.6	FCD	18
15	Male	8.9	Right	Temporal		NA	16
16	Male	8.9	Left	Temporal	1.7	NDD	14
17	Female	9.0	Right	Temporal	5.0	NDD	18
18	Female	12.1	Left	Temporal	6.4	NDD	5
19	Male	12.9	Right	Temporal	9.6	FCD	2
20	Female	13.6	Right	Temporal	13.6	HME	8
21	Female	14.4	Right	Temporal	14.4	FCD	24
22	Female	15.1	Right	Temporal	10.1	FCD	14
23	Female	15.2	Left	Temporal	14.6	FCD	13
24	Male	15.2	Right	Temporal	6.9	FCD	10
25	Male	15.5	Left	Temporal	9.5	UNK	16
26	Male	17.8	Right	Temporal	16.8	MTS	5
27	Male	19.1	Right	Temporal	2.2	SVM	1
28	Male	19.9	Left	Temporal	4.0	SVM	5
29	Male	20.3	Right	Temporal	4.6	LGT	5
30	Female	20.3	Right	Temporal	16.7	SVM	3
31	Male	21.2	Left	Temporal	13.3	LGT	4
32	Male	22.1	Right	Temporal	5.1	NA	6
33	Male	24.8	Left	Temporal	6.2	SVM	3
34	Male	24.8	Left	Temporal	16.0	MTS	4
35	Male	25.0	Right	Temporal	10.0	SVM	7
36	Male	25.4	Left	Temporal	1.9	LGT	12
37	Male	26.5	Left	Temporal	8.0	NDD	9
38	Female	27.4	Right	Temporal	13.4	MTS	5
39	Male	27.7	Left	Temporal	3.6	LGT	3
40	Male	29.2	Right	Temporal	6.6	SVM	4
41	Female	29.3	Left	Temporal	16.6	MTS	8
42	Female	29.6	Left	Temporal	27.6	MTS	2
43	Male	31.2	Right	Temporal	11.2	FCD	11
44	Female	31.3	Right	Temporal	10.1	MTS	6
45	Female	31.4	Left	Temporal	5.3	SVM	1
46	Female	31.9	Right	Temporal	25.6	SVM	5
47	Female	32.4	Left	Temporal	17.8	MTS	9
48	Male	34.7	Left	Temporal	12.3	MTS	4
49	Female	35.0	Right	Temporal	16.0	SVM	6
50	Male	35.5	Left	Temporal	12.5	LGT	8
51	Male	38.4	Right	Temporal	10.3	MTS	1
52	Female	38.9	Left	Temporal	32.3	MTS	7
53	Male	39.4	Right	Temporal	6.3	MTS	2

54	Female	39.8	Right	Temporal	24.0	MTS	8
55	Female	40.2	Left	Temporal	18.3	NA	5
56	Female	40.2	Right	Temporal	16.7	MTS	1
57	Female	40.3	Right	Temporal	6.4	MTS	2
58	Female	40.5	Right	Temporal	32.6	SVM	5
59	Male	40.7	Right	Temporal	30.3	LGT	4
60	Female	41.2	Right	Temporal	2.2	FCD	4
61	Female	41.6	Left	Temporal	11.1	LGT	2
62	Male	43.1	Right	Temporal	37.0	MTS	2
63	Male	43.5	Right	Temporal	19.0	MTS	5
64	Male	43.6	Left	Temporal	39.6	MTS	5
65	Male	43.8	Left	Temporal	8.8	MTS	5
66	Female	44.9	Right	Temporal	22.2	MTS	9
67	Male	46.3	Left	Temporal	31.3	NA	13
68	Female	46.3	Right	Temporal	29.7	SVM	2
69	Male	46.8	Right	Temporal	12.1	SVM	1
70	Female	47.0	Right	Temporal	21.2	LGT	6
71	Female	48.3	Right	Temporal	1.8	SVM	2
72	Male	49.2	Left	Temporal	41.1	MTS	5
73	Male	49.2	Right	Temporal	33.0	MTS	1
74	Female	51.0	Right	Temporal	45.0	MTS	2
75	Male	51.4	Right	Temporal	48.0	SVM	1
76	Male	52.7	Left	Temporal	34.7	LGT	8
77	Male	52.8	Left	Temporal	47.0	MTS	3
78	Female	52.9	Left	Temporal	42.4	MTS	3
79	Male	54.2	Left	Temporal	9.0	SVM	3
80	Female	54.4	Right	Temporal	29.4	SVM	1

Neural recordings (N = 584) were obtained from 80 tissue donors with diverse epilepsy etiologies. The sample included mesial temporal sclerosis (MTS, n = 24), structural/vascular malformations (SVM, n = 17; including cavernoma and encephalocele), focal cortical dysplasia (FCD, n = 16), hemimegalencaphaly (HME, n = 4), low-grade tumors (LGT, n = 10; including ganglioglioma and DNET), and neurodevelopmental disorders (NDD, n = 5; Rasmussen's encephalitis and Sturge-Weber syndrome). Etiology was unknown in 1 case (non-lesional) and unavailable for 5 donors.

Table S2 - Mouse datasets

Dataset	Strain	Cortical area	Age range (days)	# Cells	# Animals	Recording temp (°C)	LJP (mV)
Current study	C57BL/6	Frontal cortex	0.8-5.2	30	11	34	15
Ciganok-Hueckels et al., 2022	C57BL/6	Visual cortex	10-64	60	43	32	14
Gouwens et al., 2019	C57BL/6	Visual cortex	35-65	69	61	34	16
Kroon et al., 2019	C57BL/6	Frontal cortex	6-30	41	18	31	16.9
Oswald et al., 2008	Swiss Webster	Auditory cortex	9-29	199	50	32	15.6
Scala et al., 2021	C57BL/6	Motor cortex	36-65	25	18	25	15.3
Weiler et al., 2023	C57BL/6	Visual cortex	30-36	137	41	22.5	15.7

Summary of electrophysiological datasets from seven studies included in this study. LJP: Liquid junction potential calculated using the stationary Nernst–Planck equation (Marino et al., 2014) using LJPcalc software (https://swharden.com/LJPcalc/).

Table S3 - GLM model designs

Species	Feature	Glmm formula	Dispersion formula	# Cells	# Subjects	# Labs
human	R_N*	~ ns(age, 2) + soma_depth + (1 | subject_id)	~age	559	79	
human	Mem. time const.*	~ ns(age, 2) + soma_depth + (1 | subject_id)	~ns(age, 2)	554	70	
human	Sag ratio	~ ns(age, 2) + soma_depth + (1 | subject_id)	~age	548	71	
human	Rheobase*	~ ns(age, 2) + soma_depth + (1 | subject_id)	~ns(age, 2)	560	71	
human	AP stability	~ ns(age, 2) + soma_depth + (1 | subject_id)	~age	472	54	
human	AP thresh.	~ ns(age, 2) + soma_depth + laboratory + (1 | subject_id)	~age	500	68	2
human	AP amp.	~ ns(age, 2) + soma_depth + laboratory + (1 | subject_id)	~ns(age, 2)	499	68	2
human	AP half-width*	~ ns(age, 2) + soma_depth + (1 | subject_id)	~ns(age, 2)	500	68	
human	AP upstroke	~ ns(age, 2) + soma_depth + (1 | subject_id)	~1	500	68	
human	AP downstr.	~ ns(age, 2) + soma_depth + (1 | subject_id)	~age	500	68	
human	AP udsr	~ age + soma_depth + (1 | subject_id)	~age	500	68	
mouse	R_N*	~ ns(age, 3) + laboratory + (1 | subject_id)	~ns(age, 2)	555	240	7
mouse	Mem. time const.*	~ ns(age, 3) + laboratory + (1 | subject_id)	~ns(age, 2)	418	199	6
mouse	Sag ratio	~ ns(age, 3) + laboratory + (1 | subject_id)	~age	341	181	6
mouse	Rheobase*	~ ns(age, 3) + laboratory + (1 | subject_id)	~ns(age, 2)	378	172	6
mouse	AP stability	~ ns(age, 3) + laboratory + (1 | subject_id)	~age	136	92	4
mouse	AP thresh.	~ ns(age, 3) + laboratory + (1 | subject_id)	~1	555	240	7
mouse	AP amp.	~ ns(age, 3) + laboratory + (1 | subject_id)	~age	552	239	7
mouse	AP half-width	~ ns(age, 3) + laboratory + (1 | subject_id)	~ns(age, 2)	415	199	6
mouse	AP upstroke	~ ns(age, 3) + laboratory + (1 | subject_id)	~age	142	94	4
mouse	AP downstr.	~ ns(age, 2) + (1 | subject_id)	~age	142	94	
mouse	AP udsr	~ age + laboratory	~age	142	94	4

Human and mouse final model designs with sample size and number of levels for fixed and random effects.
*Feature log-transformed prior to fitting.

Table S4 - Mouse dataset intracellular solutions

Publication	K-gluconate	KCl	HEPES	EGTA	Mg-ATP	Na-GTP	Na_2phosphocreatine	biocytin (%)
Current study	110	10	10		4	0.4	10[2]	0.5
Ciganok-Heuckels et al., 2022	100	20	10		4	0.3	10	0.5
Gouwens et al., 2019	126	4	10	0.3	4	0.3	10	0.5
Kroon et al., 2019	148	1	10		4	0.4	4[2]	0.2
Oswald et al., 2008	130	5	10		4	0.3	10	0.5
Scala et al, 2021[1]	111	4	10	0.2	4	0.3	5	0.5
Weiler et al., 2023	126	4	10		4	0.3	10	0.3-0.5[3]

All studies included in the mouse dataset employed very similar K-gluconate based intracellular solutions. [1]Also included RNAse inhibitor (1U/mL), [2]K_2phosphocreatine, [3]neurobiotin.

Table S5 - Mouse dataset extracellular solutions

Publication	NaCl	KCl	NaH_2PO_4	D-glucose	$MgCl_2$	$CaCl_2$	$NaHCO_3$
Current study	126	3	1.25	10	1	2	26
Ciganok-Heuckels et al., 2023, Oswald et al., 2008	125	2.5	1.25	25	1	2	25
Gouwens et al., 2019[1]	126	2.5	1.25	12.5	1[2]	2	26
Kroon et al., 2019	126	3	1.25	10	1.5	1.6	26
Scala et al., 2021	125	2.5	1.25	11.1	1	2	25
Weiler et al., 2023	127	2.5	1.25	10	2	2	26

All studies included in the mouse dataset employed very similar extracellular solutions. [1]Also included kynurenic acid and picrotoxin, [2]$MgSO_4$.